ELSEVIER

Contents lists available at ScienceDirect

# Agricultural Water Management

journal homepage: www.elsevier.com/locate/agwat





# Estimation of crop evapotranspiration from MODIS data by combining random forest and trapezoidal models

Pengyu Hao, Liping Di \*, Liying Guo

Center for Spatial Information Science and Systems, George Mason University, Fairfax, VA, USA

#### ARTICLE INFO

Keywords: ET Remote sensing ESVEP Machine learning Nebraska

#### ABSTRACT

Evapotranspiration (ET) is an important parameter for crop growth monitoring and land surface modeling. This paper proposed a new workflow, namely ESVEP-RF, to calculate ET during the crop growing season using MODIS data by combining the advantages of the trapezoidal model and Random Forest (RF) algorithm. In ESVEP-RF, the endmember-based soil and vegetation energy partitioning (ESVEP) model was first used to calculate a series of parameters from MODIS and meteorological inputs, and then all parameters derived from remote sensing data, meteorological data and ESVEP models were used as inputs to the RF algorithm for latent heat flux (LE) calculation. In-situ data of 12 years (2003-2012, 2018 and 2019) from five flux towers located in Nebraska (NE) and Michigan (MI) were used to test the performance of ESVEP-RF, and results showed that ESVEP-RF had great potential to accurately calculate ET when the number of training samples was sufficient and representative. In 2010 and 2011, R<sup>2</sup> of LE were around 0.8 and RMSE were around 70 W/m<sup>2</sup>, which outperformed original ESVEP model results. This indicated that the RF algorithm could better describe the non-linear correlation between in LST/FVC space endmembers and LE. Among all parameters, LAI, PLEv and R-vw had high contribution with percentage importance of 18.49%, 15.71% and 13.57%, respectively. Furthermore, all samples between 2003 and 2012 collected from the three NE sites were used to train RF models and then calculate LE for both NE and MI sites in 2018 and 2019. In NE sites, RMSE was around 65 W/m<sup>2</sup> and R<sup>2</sup> was around 0.8. In MI sites, it was noted that no samples from these sites were included in the training data set, and RMSE was around 70 W/m<sup>2</sup> and R<sup>2</sup> was higher than 0.7. These results showed the potential of ESVEP-RF for providing up-to-date ET information

### 1. Introduction

Evapotranspiration (ET) is the loss of water from the land surface to atmosphere, which is a key component in water cycle and energy balance systems (Burt et al., 2005; Di, 1991; Farahani et al., 2007; Moran et al., 1994; Pereira et al., 2015). Additionally, ET is also a major hydrological variable in agricultural applications, since accurate ET calculation provides important information for crop growth monitoring and crop yield prediction (Allen et al., 2007; Anderson et al., 2007; Knipper et al., 2020; USGS, 2010; Wang and Dickinson, 2012).

Remote sensing-based methods have been widely used for cropland ET calculation and monitoring from regional to global scale (Jéffersonde et al., 2020; Jiang et al., 2020; Knipper et al., 2020; Liu et al., 2019; Mu et al., 2007, 2011; Xue et al., 2020; Yu et al., 2019), and can be categorized into three groups based on their principles: (1) surface energy balance methods, (2) surface water balance methods, and (3) land

surface temperature (LST)/fractional vegetation cover (FVC) feature space methods (Carlson, 2007; Li et al., 2009; Senay, 2008; Su, 1988). Among these methods, LST/FVC feature space methods are advantageous in ET calculation because they avoid complex aerodynamic and land surface resistance parameterization required for other methods (Jiang et al., 2009; Kimball and Running, 2016; Leng et al., 2017).

The hypothesis of the LST/FVC feature space methods is that remotely sensed LST and FVC of all clear-sky pixels in an image could be used to generate a two dimensional space, and the envelope of these pixels could constitute a physically meaningful triangle or trapezoid (Carlson, 2007). The edges of the triangle or trapezoid represent extreme wet/dry situations in the image and the vertices are called dry/wet endmembers. Consequently, one challenge in using the LST/FVC methods to calculate ET is the determination of wet and dry edges. An LST/FVC feature space is only applicable in the same meteorological and terrain conditions. Therefore, the methods are not suitable at a

E-mail addresses: phao@gmu.edu (P. Hao), ldi@gmu.edu (L. Di), lguo2@gmu.edu (L. Guo).

<sup>\*</sup> Corresponding author.

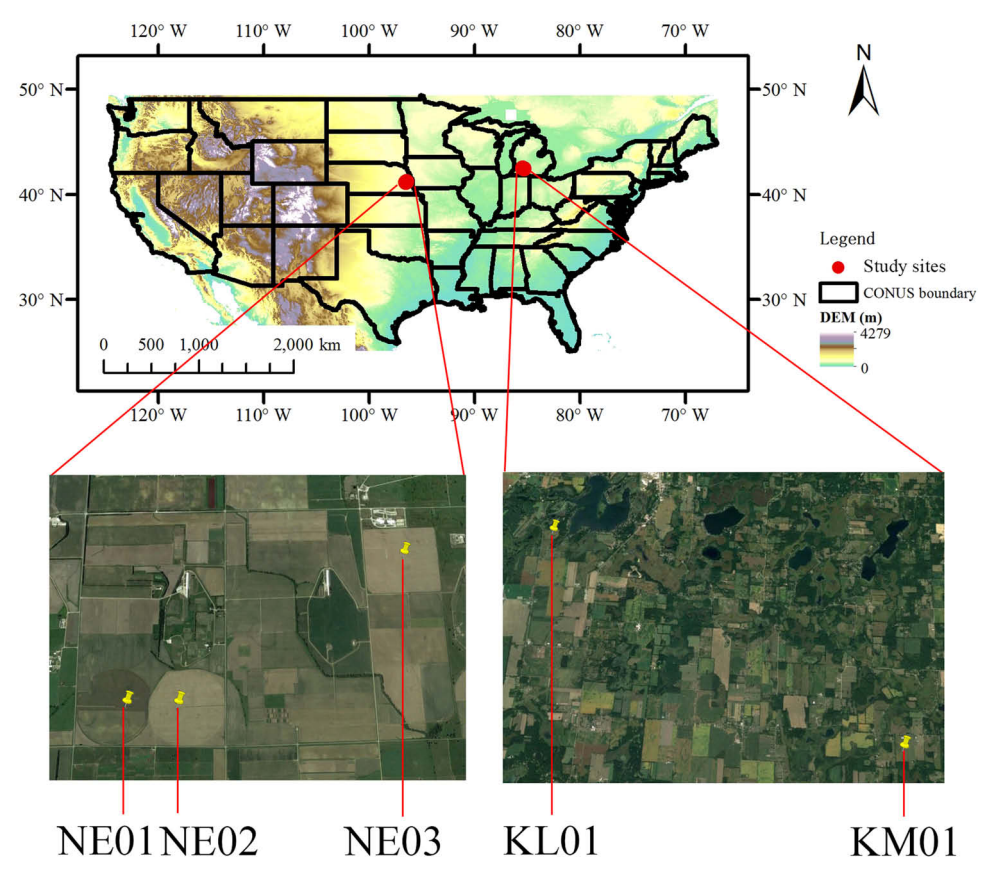


Fig. 1. Location of the five test sites used in this study. In the Figure, NE01, NE02, NE03, KL01 and KM01 denote AmeriFlux towers US-Ne1, US-Ne2, US-Ne3, US-KL1 and US-KM1, respectively.

continental or global scale where meteorological and terrain conditions vary greatly and wet/dry edges are difficult to determine from remote sensing data alone. As there have been several regionally gridded meteorological products openly available, such as the North American Land Data Assimilation System (NLDAS) data at 0.125° spatial resolution (Xia et al., 2015), it is possible to combine remote sensing data with meteorological data to determine the wet/dry edges of LST/FVC feature space for each pixel in a remote sensing image based on the surface energy balance theory. With this combination, the applicability of LST/FVC methods could be extended to global scale.

Another challenge of LST/FVC feature space methods is how to separate soil evaporation (ETs) and vegetation transpiration (ETv). Some conventional two-source trapezoidal models have been proposed based on the assumption that vegetation temperature (Tv) and soil temperature (Ts) vary concurrently with soil moisture variation, and ETv and ETs vary together with Ts and Tv variation in the LST/FVC trapezoid (Long and Singh, 2012; Sun, 2015; Yang et al., 2015). Therefore, variation speed of ETv and ETs calculated from these conventional trapezoidal models are nearly equal (Jiang et al., 2019; Tang and Li, 2017). However, the variation rate of ETv and ETs should be different because ETv primarily uses water from the root-zone layer while ETs primarily uses water from the surface soil layer, and the soil moisture of the two layers are different in the most cases. To overcome this drawback, Tang and Li (2017) proposed an end-member-based soil and vegetation energy partitioning (ESVEP) model, which showed good potential for separating ETv and ETs by using a two-stage trapezoid procedure. First, ETs would drop from potential ETs to zero if water content in the surface soil layer decreases from sufficiency to zero, and ETv would remain to be potential ETv if the water content in the root zone layer remains sufficient. Second, ETv would drop from potential ETv to zero if water content in the root zone layer decreases to wilting point, and ETs would keep at zero if soil water content in the surface soil

layer remains at zero. Actual ETs and ETv of a pixel are calculated based on the linear ratio between the pixel location and endmembers in the LST/FVC feature space. The ESVEP model has shown good potential for calculating ET using satellite observations (Jiang et al., 2019). However, the relationship between actual ET (ETv and ETs) and potential ET (PETv and PETs) may be not linear. Therefore, a non-linear approach should be tested in the end-member-based two-source trapezoidal models for ET calculation.

Machine learning (ML) approaches provide new ways to deal with non-linearity in the construction of models for classification and regression (Virnodkar et al., 2020), and have been proved to be effective in agricultural remote sensing applications, such as crop type classification, plant biophysical and biochemical parameters estimation, crop water stress detection, and yield prediction (Filgueiras et al., 2020; Hao et al., 2020b; Loozen et al., 2020; Oliveira et al., 2020; Rahman and Di, 2020; Sun et al., 2020a, 2020b; Xu et al., 2020; Zhang et al., 2019). As for ML-based ET estimation, most studies used land surface parameters calculated from remote sensing data (such as albedo, land surface temperature, vegetation indices, etc.) and meteorological parameters (such as wind speed, vapor pressure deficit, etc.) as inputs (Chia et al., 2020; Virnodkar et al., 2020), but very few studies used parameters calculated from water cycle and energy balance mechanism as inputs for ML. Therefore, objectives of this study are: (1) using ML methods to fill the gap between parameters generated in two-source trapezoidal models and actual ET, and (2) estimating the potential of using historical data as training samples to calculate corn and soybean ET by combining ESVEP and ML approaches at five AmeriFlux cropland tower sites in Nebraska and Michigan. The rest of this paper is organized as follows: Section 2 discusses the materials and methods of this study; Section 3 presents research results; Section 4 analyzes and discusses the results, and Section 5 provides the conclusion of this study.

**Table 1**Energy balance closure of the ground-truth data.

	Intercept (W/m²)	Slope	R <sup>2</sup>
FluxNET-US-NE01	1.70	0.77	0.93
FluxNET-US-NE02	2.09	0.80	0.94
FluxNET-US-NE03	20.99	0.97	0.67
AmeriFlux-US-NE01	3.09	0.77	0.94
AmeriFlux-US-NE02	4.27	0.79	0.94
AmeriFlux-US-NE03	5.72	0.81	0.95

Note: This table reports the Regression coefficients of LE+H against Rn-G, using all the valid hourly data for each site. As the AmeriFlux data of the sites KL01 and KM01 did not provide the in-situ Rn, we just evaluated the EBC of the FluxNET and AmeriFLUX of US-NE01, US-NE02 and US-NE03.

Table 2
MODIS products used in this study.

	Spatial resolution (Meter)	Temporal resolution (Day)	Included parameters	Derived parameters
MOD09GA	500	Daily	Surface reflectance of MODIS bands 1–7	NDVI, albedo
MOD11A1	500	Daily	LST, spectral emissivity of MODIS bands 31 and 32	broadband emissivity
MOD15A2	1000	4-day	LAI	

### 2. Data sets and methodology

#### 2.1. Study area and flux data

The study area is located in Nebraska (NE) and Michigan (MI), both part of the U.S. Corn Belt, with corn and soybean as the two dominant crops. In-situ data of five AmeriFlux tower cropland sites in Nebraska and Michigan, namely US-Ne1, US-Ne2 and US-Ne3, US-KL1 and US-KM1, are used in this study. The locations of these five sites are shown in Fig. 1. These sites have different crop rotation and irrigation conditions: US-Ne1, US-KL1 and US-KM1 are irrigated continuous corn sites,

US-Ne2 is an irrigated corn-soybean rotation site, and US-Ne3 is a rainfed corn-soybean rotation site. The mean annual precipitation of the Nebraska and Michigan sites are around 790 mm and 960 mm, and the mean annual temperatures are around 10  $^{\circ}$ C and 18  $^{\circ}$ C, respectively.

The hourly in-situ data from 2003 to 2012 for the three Nebraska sites were downloaded from the FLUXNET data portal (https://fluxnet. org/). The data sets were gap filled and passed the quality control checks (Pastorello et al., 2020). The latent heat flux (LE) corrected by the energy balance closure correction factor (LE\_CORR) corresponding to the satellite overpass time is used as in-situ observed LE in this study, and only the data from DOY 101 to DOY 300 which cover the growing season of corn and soybean are used. In addition, hourly in-situ data for year 2018 and 2019 are downloaded from AmeriFlux data portal (https://ameriflux.lbl.gov/). In-situ flux data for 2018 and 2019 are the original observations, which have not been corrected, but these are the only datasets we can acquire in these two years. We evaluated the energy balance closure of the ground-truth data using the regression correlation of Rn-G and LE + H (Wilson et al., 2002), and the results were shown in Table 1. The in-situ data for the three NE sites are available in both 2018 and 2019, and for the two MI sites, the data were only available in 2018. As we use MODIS Terra data to calculate LE, we only use in-situ LE observations at the satellite overpass time (10:30 am local time, which is 16:30 UTC time for the three NE sites and 15:30 UTC time for the two MI sites). The three NE sites provide hourly in-situ data so that we used the data recorded for 10:00-11:00 am as in-situ data; MI sites provide half-hourly data and we used the average value of records between 10:00 and 11:00 am. Furthermore, all samples which were labeled as cloud-covered in MODIS products were removed from sample dataset.

### 2.2. Earth observation and gridded meteorological data

### 2.2.1. MODIS data

MODIS products used in this study include land surface reflectance (MOD09GA), LST (MOD11A1), and leaf area index (LAI) (MOD15A2). The temporal and spatial resolution of the three MODIS products and parameters derived from MODIS data are shown in Table 2. Broadband emissivity was calculated from spectral emissivity of MODIS bands 31

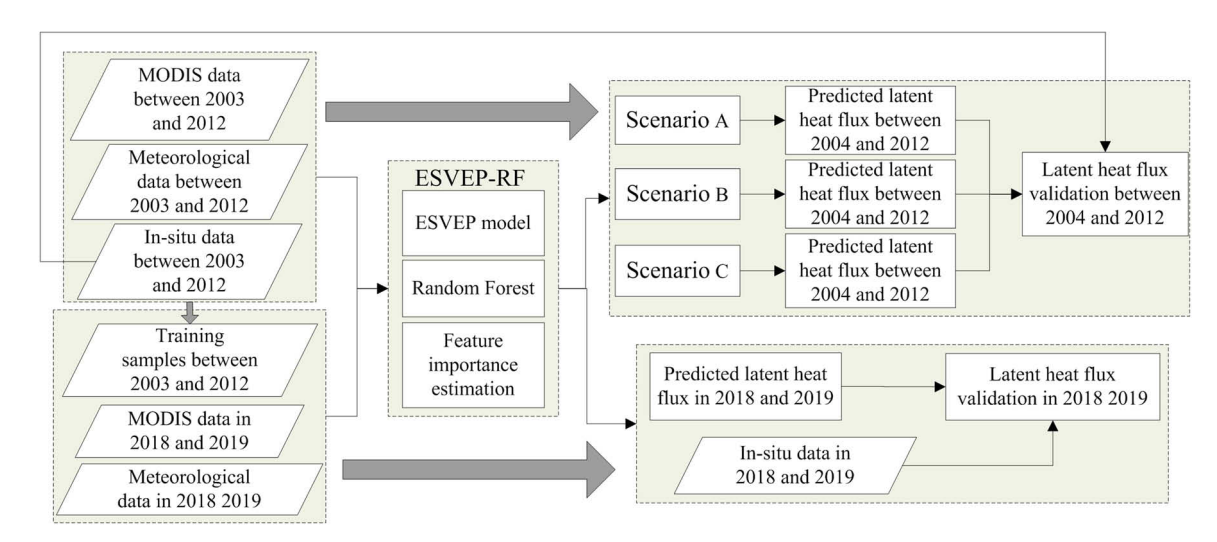


Fig. 2. Flowchart of this study. The upper-left box indicates the data used for training and testing experiments between 2003 and 2012, bottom-left box indicates the data used for training and testing experiments in 2018 and 2019. Big arrows in the figure present that the data listed in the left-boxes are processed with the ESVEP-RF, for the upper-right box, three scenarios are designed for the data between 2003 and 2012, and the LE calculation results are verified, for the bottom-right box, training samples collected between 2003 and 2012 are used to train the ESVEP-RF models and the model are used for LE calculation in 2018 and 2019. In addition, the thin arrows are the detailed data flow. For example, MODIS data, meteorological data and ground truth data are used to train ESVEP-RF model of the three scenarios, and we then acquired LE calculation results of these three scenarios, the results are then verified using the ground truth data. In is notable that when calculating the LE of the target years, only training samples of the previous years are used to train ESVEP-RF models. For instance, ground truth samples between 2003 and 2009 were used to train the machine learning models when trying to calculate LE in 2010.

**Table 3**Description of the three experiments designed to estimate The combined ESVEP and RF method for ET calculation.

	Description	Expected result	Examples
Scenario A	Training samples are all historical samples before the testing year, all three NE sites are included in both training and validation samples	Nine-year predicted LE (between 2004 and 2012)	When predicting ET of site NE01 in 2012, the training samples are all samples between 2003 and 2011 for all three NE sites; and when predicting ET of site NE01 in 2010, the training samples are all samples between 2003 and 2009 for all three NE sites.
Scenario B	Training samples are all historical samples before the testing year, training and testing samples are from different sites	Nine-year predicted LE (between 2004 and 2012)	When predicting ET of site NE01 in 2012, the training samples are all samples between 2003 and 2011 of NE02 and NE03 sites; and when predicting ET of site NE01 in 2010, the training samples are all samples between 2003 and 2009 of NE02 and NE03 sites.
Scenario C	Training samples are all historical samples before the testing year, and irrigation site and rainfed site are separated	Nine-year predicted LE (between 2004 and 2012)	When predicting ET of site NE01 in 2012, the training samples are all samples between 2003 and 2011 of NE01 and NE02 sites (irrigation sites), and when predicting ET of site NE03 in 2010, the training samples are all samples between 2002 and 2011 of NE03 site (rainfed sites).

and 32 using method reported by Liang (2004); land surface albedo was calculated from surface reflectance of MODIS bands 1–7 using method reported by Liang (2001). NDVI was calculated from spectral reflectance of MODIS bands 1 and 2 (Rouse et al., 1974). Finally, all MODIS data

were resampled to 1 km using the GDAL package for Python. The MODIS Terra satellite overpasses land surface at 10:30 am local time daily, so that in-situ LE corresponding to the satellite overpass time was used as ground truth LE. As some MODIS data were covered by clouds, cloud-covered samples were not included in the sample set because MODIS LST observation was not available. As we focus on crop ET calculation during the growing season, all MODIS data between DOY 101 and 300 between the years 2003–2012 and 2019 were collected in this study.

### 2.2.2. Meteorological data

The hourly gridded meteorological data used in this study is NLDAS-2 File A data (Xia et al., 2012). The dataset covers the conterminous US (CONUS) since 1979 at spatial resolution of 0.125°. The hourly downwards longwave radiation, downwards shortwave radiation, surface pressure, 2-m above ground specific humidity, 2-m above ground temperature and wind speed between the years 2003 and 2012 were used in this study. Another data source of meteorological data is the National Weather Model Service (NWM, https://nomads.ncep.noaa.gov/pub/da ta/nccf/com/nwm/prod/), which is an hourly analysis and forecast system running over the conterminous US (NOAA-OWP, 2016) at 500 m spatial resolution. In this study, both NLADS and NWM data were resampled to 1 km using the Bi-linear algorithms with the MODIS data as reference image, the image resampling operation was implemented using the GDAL package for Python. As the meteorological data used in this study are collected from different data sources (NLDAS data between 2003 and 2012, and NWM data for 2018 and 2019), and the original spatial resolution of the two data sources are different, the inconsistencies between the two meteorological datasets may slightly affect LE calculation result in 2018 and 2019.

### 2.3. Flowchart of this study

Fig. 2 shows the data processing flowchart of this study. We selected Random Forest (RF) as the ML model in this study and then combined ESVEP and RF (ESVEP-RF) to calculate ET. Importance of individual features generated from remote sensing data, meteorological data and ESVEP model were firstly estimated using the Gini index calculated from RF. Next, two experiments were designed to evaluate the performance of ESVEP-RF for ET calculation. The first experiment was designed to evaluate the performance of ESVEP-RF for ET calculation with data

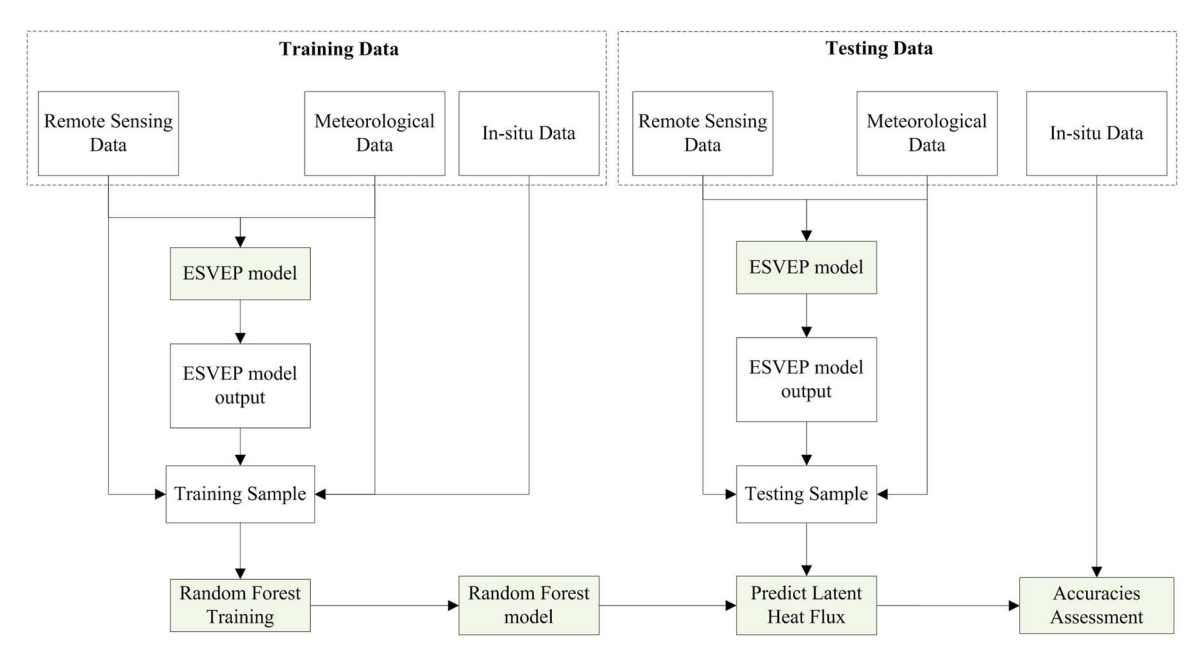


Fig. 3. Data Processing flowchart of ESVEP-RF.

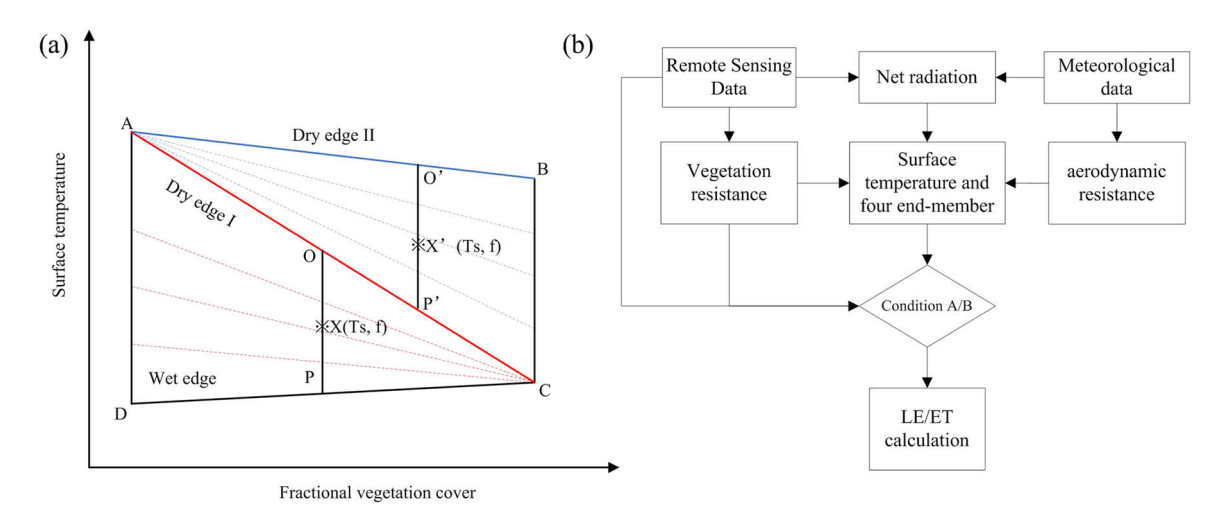


Fig. 4. ESVEP model and the dataflow for parameter generation. (a) Surface temperature versus fractional vegetation cover trapezoid space. The edge CD denotes wet edge; as triangle ACD denotes the condition that soil zone water is sufficient, edge AC denotes the dry edge of the triangle ACD, and we labeled the edge as Dry edge I in the figure; similarly, triangle ABC denotes the condition that the plant is water-stressed, edge AB denotes the dry edge of the triangle ABC and we labeled the edge as Dry edge II. (b) Workflow of parameter calculation using ESVEP model.

**Table 4** Input and output parameters for ESVEP model.

AGDD: Accumulated Growing Degree Day  Veghgt: Vegetation Height Remote Sensing Input Leaf Area Index NDVI SRb1: Surface Reflectance of Band 1 (Red) SRb2: Surface Reflectance of Band 2 (NIR) SRb3: Surface Reflectance of Band 2 (Blue) SRb4: Surface Reflectance of Band 2 (Green) SRb5: Surface Reflectance of Band 2 (Green) SRb5: Surface Reflectance of Band 2 (SWIR1) SRb6: Surface Reflectance of Band 2 (SWIR2)  albedo s: soil albedo Soil emissivity Ts: soil temperature Ls: longwave radiation from soil Rns: net radiation of vegetation  Gs: soil heat flux R-vw: canopy resistance at well-watered condition R-vw: canopy resistance at zero-soil-water condition R-as: aerodynamic resistance of vegetation Band 2 (SWIR2)	Input Parameters	Out parameters
Shortwave Radiation DLward: Downward Longwave Radiation Windspeed Windspeed Tah: 2 m-Air Temperature Rh: Relative Humidity AGDD: Accumulated Growing Degree Day Veghgt: Vegetation Height Remote Sensing Input Leaf Area Index NDVI SRb1: Surface Reflectance of Band 1 (Red) SRb2: Surface Reflectance of Band 2 (Blue) SRb3: Surface Reflectance of Band 2 (Green) SRb5: Surface Reflectance of Band 2 (SWIR1) SRb6: Surface Reflectance of Band 2 (SWIR2) SRb7: Surface Reflectance of Band 2 (SWIR3) FVC: fractional vegetation Cover Emissivity Tw: tolongwave radiation from vegetation Ts: soil albedo Soil emissivity Ts: soil temperature Ls: longwave radiation from soil Rnv: net radiation of vegetation Gs: soil heat flux R-vw: canopy resistance at well-watered condition R-sv: aerodynamic resistance of soil R-av: aerodynamic resistance of vegetation T*: critical surface temperature to decide whether the pixel in dry triangle or wet triangle Tsd: temperature of dry vegetation end-member Tvw: temperature of wet vegetation end-member Tvw: temperature of wet vegetation LE LEs: actual vegetation LE LEs: actual vegetation LE LEs: actual vegetation LE LES: actual vegetation LE	Meteorological Input	$\Delta$ : slope of saturated water vapor pressure
DLward: Downward Longwave Radiation  Windspeed VPD  Tah: 2 m-Air Temperature Rh: Relative Humidity  AGDD: Accumulated Growing Degree Day Veghgt: Vegetation Height Remote Sensing Input Leaf Area Index NDVI SRb1: Surface Reflectance of Band 1 (Red) SRb2: Surface Reflectance of Band 2 (NIR) SRb3: Surface Reflectance of Band 2 (Green) SRb4: Surface Reflectance of Band 2 (Green) SRb5: Surface Reflectance of Band 2 (SWIR1) SRb7: Surface Reflectance of Band 2 (SWIR2) SRb7: Surface Reflectance of Band 2 (SWIR3) FVC: fractional vegetation cover Emissivity LST: Land Surface Temperature Emissivity Tv: fraction vegetation from vegetation albedo Lv: longwave radiation from vegetation transmittance albedo Sv: soil albedo Soil emissivity Ts: soil temperature Soil emissivity Ts: soil temperature Soil emissivity Ts: soil temperature at well-watered condition R-av: canopy resistance at zero-soil-water condition R-av: aerodynamic resistance of vegetation T*: critical surface temperature to decide whether the pixel in dry triangle or wet triangle Tsd: temperature of dry vegetation end-member Tvw: temperature of dry vegetation end-member Tvw: temperature of wet vegetation end-member PLEv: potential of transmittance albedo Ts: carcual vegetation LE LEs: actual vegetation LE LEs: actual vegetation LE	DSward: Downward	Air emissivity
Radiation Windspeed VPD Tah: 2 m-Air Temperature Rh: Relative Humidity AGDD: Accumulated Growing Degree Day Veghgt: Vegetation Height Remote Sensing Input Leaf Area Index NDVI SRb1: Surface Reflectance of Band 1 (Red) SRb2: Surface Reflectance of Band 2 (NIR) SRb3: Surface Reflectance of Band 2 (Blue) SRb4: Surface Reflectance of Band 2 (Green) SRb5: Surface Reflectance of Band 2 (Green) SRb5: Surface Reflectance of Band 2 (SWIR1) SRb7: Surface Reflectance of Band 2 (SWIR2) SRb7: Surface Reflectance of Band 2 (SWIR3) FVC: fractional vegetation cover Emissivity LST: Land Surface Temperature Emissivity Tv: conopy resistance at well-watered condition R-as: aerodynamic resistance of vegetation T*: critical surface temperature to decide whether the pixel in dry triangle or wet triangle Tsd: temperature of dry soil end-member Tvw: temperature of wet vegetation end-member Tvw: temperature of wet vegetation end-member Tvw: temperature of wet vegetation LE PLEs: potential soil LE LEs: actual vegetation LE LEs: actual vegetation LE	Shortwave Radiation	
Tah: 2 m-Air Temperature Rh: Relative Humidity  AGDD: Accumulated Growing Degree Day  Veghgt: Vegetation Height Remote Sensing Input Leaf Area Index NDVI SRb1: Surface Reflectance of Band 1 (Red) SRb2: Surface Reflectance of Band 2 (NIR) SRb3: Surface Reflectance of Band 2 (Blue) SRb4: Surface Reflectance of Band 2 (Green) SRb5: Surface Reflectance of Band 2 (SWIR1) SRb6: Surface Reflectance of Band 2 (SWIR2) SRb7: Surface Reflectance of Band 2 (SWIR3) FVC: fractional vegetation  T*: critical surface temperature to decide whether the pixel in dry triangle or wet triangle Tsd: temperature of dry soil end-member Tvw: temperature of wet vegetation end-member PLEv: potential soil LE LEs: actual vegetation LE LEs: actual vegetation LE	=	γ: psychrometric constant
Tah: 2 m-Air Temperature Rh: Relative Humidity  AGDD: Accumulated Growing Degree Day Veghgt: Vegetation Height Remote Sensing Input Leaf Area Index NDVI SRb1: Surface Reflectance of Band 1 (Red) SRb2: Surface Reflectance of Band 2 (NIR) SRb3: Surface Reflectance of Band 2 (Green) SRb5: Surface Reflectance of Band 2 (SWIR1) SRb6: Surface Reflectance of Band 2 (SWIR2) SRb7: Surface Reflectance of Band 2 (SWIR3) FVC: fraction vegetation vegetation transmittance  T**: critical surface temperature  T**: critical surface temperature to decide whether the pixel in dry triangle or wet triangle  Tw: temperature of wet soil end-member  Tvw: temperature of wet vegetation end-member  Tvw: temperature of wet vegetation end-member  Tvw: temperature of wet vegetation LE PLEs: potential soil LE LEs: actual vegetation LE LEs: actual vegetation LE	Windspeed	Lv: longwave radiation from vegetation
Rh: Relative Humidity  AGDD: Accumulated Growing Degree Day  Veghgt: Vegetation Height Remote Sensing Input Leaf Area Index NDVI SRb1: Surface Reflectance of Band 1 (Red) SRb2: Surface Reflectance of Band 2 (NIR) SRb3: Surface Reflectance of Band 2 (Blue) SRb4: Surface Reflectance of Band 2 (Green) SRb5: Surface Reflectance of Band 2 (SWIR1) SRb6: Surface Reflectance of Band 2 (SWIR2) SRb7: Surface Reflectance of Band 2 (SWIR2) SRb7: Surface Reflectance of Band 2 (SWIR3) FVC: fractional vegetation  Cover Emissivity LST: Land Surface Temperature Emissivity Tv: canopy resistance at well-watered condition R-as: aerodynamic resistance of vegetation T*: critical surface temperature to decide whether the pixel in dry triangle or wet triangle Tsd: temperature of dry soil end-member Tvw: temperature of wet soil end-member Tvw: temperature of wet vegetation end-member PLEv: potential vegetation LE PLEs: potential soil LE LE: actual vegetation LE LEs: actual vegetation LE	VPD	albedo
AGDD: Accumulated Growing Degree Day  Veghgt: Vegetation Height Remote Sensing Input Leaf Area Index NDVI SRb1: Surface Reflectance of Band 1 (Red) SRb2: Surface Reflectance of Band 2 (NIR) SRb3: Surface Reflectance of Band 2 (Blue) SRb4: Surface Reflectance of Band 2 (Green) SRb5: Surface Reflectance of Band 2 (SWIR1) SRb6: Surface Reflectance of Band 2 (SWIR2) SRb7: Surface Reflectance of Band 2 (SWIR3) FVC: fractional vegetation cover Emissivity LST: Land Surface Temperature Emissivity  Tvs: citical surface fined-member Tvd: temperature of wet vegetation end-member Tvw: temperature of wet vegetation end-member PLEv: potential soil LE LEs: actual vegetation LE LEs: actual vegetation LE LES: actual vegetation LE  LES: actual vegetation LE  Soil emissivity Ts: soil temperature at well-watered condition R-av: canopy resistance at zero-soil-water condition R-av: aerodynamic resistance of vegetation T*: critical surface temperature to decide whether the pixel in dry triangle or wet triangle Tsd: temperature of dry vegetation end-member Tvw: temperature of wet vegetation end-member Tvw: temperature of wet vegetation LE LEs: actual vegetation LE	Tah: 2 m-Air Temperature	Fv: fraction vegetation cover
Degree Day  Veghgt: Vegetation Height Remote Sensing Input Leaf Area Index NDVI SRb1: Surface Reflectance of Band 1 (Red) SRb2: Surface Reflectance of Band 2 (NIR) SRb3: Surface Reflectance of Band 2 (Blue) SRb4: Surface Reflectance of Band 2 (Green) SRb5: Surface Reflectance of Band 2 (SWIR1) SRb6: Surface Reflectance of Band 2 (SWIR2) SRb7: Surface Reflectance of Band 2 (SWIR3) FVC: fractional vegetation cover Emissivity LST: Land Surface Temperature Emissivity Trs: citical surface few tesperature of wet soil end-member Tractional vegetation Trs: citical soil LE LEs: actual vegetation LE LEs: actual vegetation LE  LS: longwave radiation from soil Rns: ret radiation of vegetation from soil Rns: net radiation of vegetation from soil Rns: net radiation of vegetation from soil Rns: net radiation of soil Rns: net radiation of vegetation from soil Rns: net radiation of soil Rns: net radiation from soil Rns: net radiation of soil	Rh: Relative Humidity	$\tau_{\text{sw}}\text{:}$ canopy shortwave radiation transmittance
Veghgt: Vegetation Height Remote Sensing Input Leaf Area Index NDVI SRb1: Surface Reflectance of Band 1 (Red) SRb2: Surface Reflectance of Band 2 (NIR) SRb3: Surface Reflectance of Band 2 (Blue) SRb4: Surface Reflectance of Band 2 (Green) SRb5: Surface Reflectance of Band 2 (SWIR1) SRb6: Surface Reflectance of Band 2 (SWIR2) SRb7: Surface Reflectance of Band 2 (SWIR3) FVC: fractional vegetation cover Emissivity LST: Land Surface Temperature Emissivity Tvw: temperature of wet vegetation end-member Tvw: temperature of wet vegetation LE PLEs: potential vegetation LE LEs: actual vegetation LE LEs: actual vegetation LE LES: actual vegetation from soil Rns: soil temperature  Scil emissivity Ts: soil temperature Ls: longwave radiation from soil Rnv: net radiation of vegetation from soil Rnv: net radiation of vegetation for soil Rnv: net radiation from soil Rnv: net radiation from soil Rnv: net radiation of vegetation for soil Rnv: net radiation from soil Rns: net radiation from soil Rnv: net radiation from soil Rns: net radiation from soil Rns: net radiation from soil Rns: net radiation from soil Rnv: net radiation from soil Rns: net radiation from soil Rns: net radiation of vegetation Fnv: net radiation for soil		albedo_s: soil albedo
Remote Sensing Input Leaf Area Index NDVI SRb1: Surface Reflectance of Band 1 (Red) SRb2: Surface Reflectance of Band 2 (NIR) SRb3: Surface Reflectance of Band 2 (Blue) SRb4: Surface Reflectance of Band 2 (Green) SRb5: Surface Reflectance of Band 2 (SWIR1) SRb6: Surface Reflectance of Band 2 (SWIR2) SRb7: Surface Reflectance of Band 2 (SWIR3) FVC: fractional vegetation cover Emissivity LST: Land Surface Temperature Emissivity Triv: temperature of wet vegetation end-member Tvw: temperature of wet vegetation end-member PLEv: potential vegetation LE LEs: actual vegetation LE LEs: actual vegetation LE		Soil emissivity
NDVI SRb1: Surface Reflectance of Band 1 (Red) SRb2: Surface Reflectance of Band 2 (NIR) SRb3: Surface Reflectance of Band 2 (Blue) SRb4: Surface Reflectance of Band 2 (Green) SRb5: Surface Reflectance of Band 2 (SWIR1) SRb6: Surface Reflectance of Band 2 (SWIR2) SRb7: Surface Reflectance of Band 2 (SWIR3) FVC: fractional vegetation cover Emissivity LST: Land Surface Temperature Emissivity Triv: temperature of wet vegetation end-member PLEv: potential vegetation LE LEs: actual vegetation LE LEs: actual vegetation LE LES: actual vegetation LE LES: actual vegetation Revv: canopy resistance at well-watered condition R-vw: canopy resistance at zero-soil-water condition R-vd: canopy resistance of soil R-vd: canopy resistance of soil R-vd: canopy resistance at zero-soil-water condition R-vd: canopy resistance at vell-watered condition R-vd:	Remote Sensing Input	Ts: soil temperature
SRb1: Surface Reflectance of Band 1 (Red) SRb2: Surface Reflectance of Band 2 (NIR) SRb3: Surface Reflectance of Band 2 (Blue) SRb4: Surface Reflectance of Band 2 (Green) SRb5: Surface Reflectance of Band 2 (SWIR1) SRb6: Surface Reflectance of Band 2 (SWIR2) SRb7: Surface Reflectance of Band 2 (SWIR2) SRb7: Surface Reflectance of Band 2 (SWIR3) FVC: fractional vegetation cover Emissivity LST: Land Surface Temperature Emissivity Trw: temperature of wet vegetation end-member Tvw: temperature of wet vegetation LE PLEs: potential soil LE LEs: actual vegetation LE LEs: actual vegetation LE LES: actual vegetation LE  R-vw: canopy resistance at well-watered condition R-vw: canopy resistance at well-watered condition R-vw: canopy resistance at vell-watered condition	Leaf Area Index	Ls: longwave radiation from soil
Band 1 (Red)  SRb2: Surface Reflectance of Band 2 (NIR)  SRb3: Surface Reflectance of Band 2 (Blue)  SRb4: Surface Reflectance of Band 2 (Green)  SRb5: Surface Reflectance of Band 2 (SWIR1)  SRb6: Surface Reflectance of Band 2 (SWIR2)  SRb7: Surface Reflectance of Band 2 (SWIR3)  FVC: fractional vegetation cover  Emissivity  LST: Land Surface Temperature  Emissivity  Tw: temperature of wet vegetation end-member Tvw: temperature of wet vegetation LE  PLEs: potential soil LE  LEs: actual vegetation LE  LES: actual vegetation LE  LES: actual vegetation LE  LES: actual vegetation LE	NDVI	Rns: net radiation of soil
Band 2 (NIR)  SRb3: Surface Reflectance of Band 2 (Blue)  SRb4: Surface Reflectance of Band 2 (Green)  SRb5: Surface Reflectance of Band 2 (SWIR1)  SRb6: Surface Reflectance of Band 2 (SWIR2)  SRb7: Surface Reflectance of Band 2 (SWIR3)  FVC: fractional vegetation cover  Emissivity  LST: Land Surface Temperature  Emissivity  Tw: temperature of wet vegetation end-member Tvd: temperature of wet vegetation end-member Tvw: temperature of wet vegetation end-member PLEv: potential vegetation LE  ElEs: actual vegetation LE  LEs: actual vegetation LE		Rnv: net radiation of vegetation
Band 2 (Blue)  SRb4: Surface Reflectance of Band 2 (Green)  SRb5: Surface Reflectance of Band 2 (SWIR1)  SRb6: Surface Reflectance of Band 2 (SWIR2)  SRb7: Surface Reflectance of Band 2 (SWIR3)  FVC: fractional vegetation cover  Emissivity  LST: Land Surface Temperature  Emissivity  Tw: temperature of wet soil end-member Tvd: temperature of dry vegetation end-member Tvd: temperature of wet vegetation end-member PLEv: potential vegetation LE  LEs: actual vegetation LE  LEs: actual vegetation LE  LES: actual vegetation LE		Gs: soil heat flux
Band 2 (Green)  SRb5: Surface Reflectance of Band 2 (SWIR1)  SRb6: Surface Reflectance of Band 2 (SWIR2)  SRb7: Surface Reflectance of Band 2 (SWIR3)  FVC: fractional vegetation cover  Emissivity  LST: Land Surface Temperature  Emissivity  Tvw: temperature of wet vegetation end-member Tvw: temperature of wet vegetation end-member PLEv: potential vegetation LE PLEs: actual vegetation LE LEs: actual vegetation LE		R-vw: canopy resistance at well-watered condition
SRb5: Surface Reflectance of Band 2 (SWIR1) SRb6: Surface Reflectance of Band 2 (SWIR2) SRb7: Surface Reflectance of Band 2 (SWIR3) FVC: fractional vegetation cover Emissivity LST: Land Surface Temperature Emissivity Tv: temperature of dry vegetation end-member Tvd: temperature of dry vegetation end-member Tvw: temperature of wet vegetation end-member PLEv: potential vegetation LE PLEs: actual vegetation LE LEs: actual vegetation LE		
Band 2 (SWIR2)  SRb7: Surface Reflectance of Band 2 (SWIR3)  FVC: fractional vegetation cover  Emissivity  LST: Land Surface Temperature  Emissivity  Tv: critical surface temperature to decide whether the pixel in dry triangle or wet triangle  Tsd: temperature of dry soil end-member  Tsw: temperature of wet soil end-member  Tvd: temperature of dry vegetation end-member  Tvw: temperature of wet vegetation end-member  PLEv: potential vegetation LE  PLEs: actual vegetation LE  LEs: actual vegetation LE	SRb5: Surface Reflectance of	**
Band 2 (SWIR3) the pixel in dry triangle or wet triangle  FVC: fractional vegetation cover  Emissivity Tsw: temperature of wet soil end-member LST: Land Surface Tvd: temperature of dry vegetation end-member Temperature  Emissivity Tvw: temperature of wet vegetation end-member PLEv: potential vegetation LE PLEs: potential soil LE LEv: actual vegetation LE LEs: actual vegetation LE		R-av: aerodynamic resistance of vegetation
FVC: fractional vegetation cover  Emissivity Tsw: temperature of wet soil end-member  LST: Land Surface Tvd: temperature of dry vegetation end-member  Temperature  Emissivity Tvw: temperature of wet vegetation end-member  PLEv: potential vegetation LE  PLEs: potential soil LE  LEv: actual vegetation LE  LEs: actual vegetation LE	SRb7: Surface Reflectance of	T*: critical surface temperature to decide whether
cover Emissivity Tsw: temperature of wet soil end-member LST: Land Surface Tvd: temperature of dry vegetation end-member Temperature Emissivity Tvw: temperature of wet vegetation end-member PLEv: potential vegetation LE PLEs: potential soil LE LEv: actual vegetation LE LEs: actual vegetation LE	Band 2 (SWIR3)	the pixel in dry triangle or wet triangle
LST: Land Surface Temperature  Emissivity Tvw: temperature of wet vegetation end-member PLEv: potential vegetation LE PLEs: potential soil LE LEv: actual vegetation LE LEs: actual vegetation LE	· ·	Tsd: temperature of dry soil end-member
Temperature Emissivity Tvw: temperature of wet vegetation end-member PLEv: potential vegetation LE PLEs: potential soil LE LEv: actual vegetation LE LEs: actual vegetation LE	Emissivity	Tsw: temperature of wet soil end-member
PLEv: potential vegetation LE PLEs: potential soil LE LEv: actual vegetation LE LEs: actual vegetation LE		Tvd: temperature of dry vegetation end-member
PLEv: potential vegetation LE PLEs: potential soil LE LEv: actual vegetation LE LEs: actual vegetation LE	•	Tvw: temperature of wet vegetation end-member
PLEs: potential soil LE LEv: actual vegetation LE LEs: actual vegetation LE	-	
LEv: actual vegetation LE LEs: actual vegetation LE		
9		
LE_all: total LE		LEs: actual vegetation LE
		LE_all: total LE

between 2003 and 2012, and there were three scenarios using different training samples (Table 3). Scenario A was designed to estimate the general performance of ESVEP-RF method; Scenario B was designed to estimate the extendibility of ESVEP-RF and Scenario C was designed to generate different RF models for irrigation and rainfed sites, and then effect of irrigation on ESVEP-RF performance was evaluated. The second experiment was using all samples acquired between in 2003 and 2012 as training samples to train RF models, and then using these RF models to calculate ET in 2018 and 2019, this experiment is designed to test the applicability of ESVEP-RF for an up-to-date ET calculation system. Finally, all ET were verified using the corresponding in-situ data, and total actual LE was verified because in-situ data do not provide ETv and ETs.

### 2.4. ESVEP-RF

Fig. 3 showed the data processing flowchart of ESVEP-RF. Remote sensing data and meteorological data were used as input in ESVEP model, and then a series of parameters were generated from ESVEP model. Parameters from remote sensing data, meteorological data and ESVEP model were combined with corresponding in-situ observed data as training/testing samples. The training samples were then used to train RF models. Next, remote sensing data, meteorological data and ESVEP model outputs of the testing samples were collected and LE of these testing samples were predicted using the RF models. Finally, in-situ LE of the testing samples were used to verify the RF predicted LE.

### 2.5. ESVEP model

The end-member-based soil and vegetation energy partitioning (ESVEP) model is based on the LST/FVC feature trapezoid space models for the actual ET calculation (Fig. 4). In the trapezoid, there are four end-members: end-members A, B, C, and D denotes dry soil, dry vegetation, wet vegetation and wet soil, and the LST of these four end-members are denoted as  $T_{\rm sd}$ ,  $T_{\rm vd}$ ,  $T_{\rm vw}$  and  $T_{\rm sw}$ . The LST/FVC feature trapezoid could be divided as two triangles. The lower triangle (triangle ACD) simulates the situation that root-zone water is sufficient and soil evaporation varies, and the upper triangle (triangle ABD) simulates the situation that vegetation is water-stressed. Generally, ET is composed by evaporation comes from soil evaporation (ETs) and vegetation transpiration (ETv), if

the LST/FVC of a pixel locates in triangle ACD, soil water content at the root zone almost remains sufficient, so that the actual canopy transpiration is nearly equal to the potential canopy transpiration, and the reduction of total ET is due mainly to the decrease of soil evaporation. If the LST/FVC of a pixel is located in triangle ABD, soil evaporation remains zero and vegetation transpiration drops from potential vegetation transpiration to zero with less root-zone water available (Jiang et al., 2019; Leng et al., 2017; Tang and Li, 2017).

For a given pixel (for example point X or X' in Fig. 4), a critical surface temperature ( $T^*$ ) is used to decide which triangle the pixels are located in (Eq. (1)),

$$T^* = \left[ T_{sd}^4 \cdot (1 - F_v) + T_{vw}^4 \cdot F_v \right]^{1/4} \tag{1}$$

where  $\boldsymbol{F}_{\boldsymbol{v}}$  is the FVC of given pixel, which is calculated as:

$$F_{v} = \left(\frac{NDVI - NDVI_{min}}{NDVI_{max} - NDVI_{min}}\right)^{2} \tag{2}$$

where NDVI is calculated from surface reflectance of Red and Near Infrared bands of MODIS data (Band 01 and Band 02).  $NDVI_{max}$  and  $NDVI_{min}$  are assigned to be 0.2 and 0.86 in this work according to Prihodko and Goward (1997). For a given pixel, if the pixel is located in triangle ACD (for example point X in Fig. 4), ETs and ETv and be calculated as:

where  $E_{s,p}$  and  $E_{v,p}$  are potential soil evaporation and vegetation transpiration, respectively, and OX and OP are lengths of the lines between points O and X and points O and P, respectively. If the pixel is located in triangle ABD (for example point X' in Fig. 4), ETs and ETv and be calculated as:

$$\begin{cases} ET_s = 0 \\ ET_v = \frac{O'X'}{O'P'} \times E_{v,p} \end{cases}$$
 (4)

where O'X' and O'P' are lengths of the lines between points O' and X' and points O' and P', respectively. Then, the  $\frac{OX}{OP}$  and  $\frac{O'X'}{O'P'}$  can be calculated as:

$$\begin{cases} \frac{OX}{OP} = \frac{(1 - F_v) \times T_{sd} + F_v \times T_{vw} - T_s}{(1 - f) \times (T_{sd} - T_{vw})} \\ \frac{O'X'}{O'P'} = \frac{(1 - F_v) \times T_{sd} - F_v \times T_{vw} - T_s}{f \times (T_{vd} - T_{vw})} \end{cases}$$
 (5)

and LST of the four end-members can be calculated as Moran et al. (1994):

$$\begin{cases} T_{sd} = \frac{r_{as} \bullet \left(R_{n,s} - G_{s}\right)}{\rho \bullet C_{p}} + T_{a} \\ T_{vd} = \frac{r_{av} \bullet R_{n,v}}{\rho \bullet C_{p}} \bullet \frac{\gamma \left(1 + r_{vd} / r_{av}\right)}{\Delta + \gamma \left(1 + r_{vd} / r_{av}\right)} - \frac{VPD}{\Delta + \gamma \left(1 + r_{vd} / r_{av}\right)} + T_{a} \\ T_{vw} = \frac{r_{av} \bullet R_{n,v}}{\rho \bullet C_{p}} \bullet \frac{\gamma \bullet \left(1 + r_{vw} / r_{av}\right)}{\Delta + \gamma \left(1 + r_{vw} / r_{av}\right)} - \frac{VPD}{\Delta + \gamma \left(1 + r_{vw} / r_{av}\right)} + T_{a} \\ T_{sw} = \frac{r_{as} \bullet \left(R_{n,s} - G_{s}\right)}{\rho \bullet C_{p}} \bullet \frac{\gamma}{\Delta + \gamma} - \frac{VPD}{\Delta + \gamma} + T_{a} \end{cases}$$

where  $R_{n,s}$  and  $R_{n,v}$  are the net radiation of soil and vegetation,  $G_s$  is soil heat flux,  $T_a$  is air temperature,  $C_p$  is volumetric heat capacity of air,  $\gamma$  is psychrometric constant,  $\Delta$  is the slope of saturated vapor pressure versus air temperature, VPD is vapor pressure deficit of air,  $r_{vw}$  and  $r_{vd}$  are canopy resistance at the well-watered and zero-soil-water, which can be set as 100/LAI and 2000~s/m;  $r_{as}$  and  $r_{av}$  are aerodynamic resistance of

soil and vegetation, which can be calculated as:

$$r_{av}(r_{as}) = \frac{\left[ ln \left( \frac{z_{u} - d}{z_{om}} \right) - \phi_{m} \right] \bullet \left[ ln \left( \frac{z_{i} - d}{z_{oh}} \right) - \phi_{h} \right]}{r^{2} - r}$$

$$(7)$$

where k is Von Karman's constant; u is wind speed;  $z_u$  and  $z_t$  are the heights of wind speed and air temperature measurements; and  $\phi_m$  and  $\phi_h$  are the stability correction functions for momentum and heat transfer, which are calculated using the method described in Dhungel et al. (2016). d is the zero-plane displacement height;  $z_{om}$  is surface momentum roughness height;  $z_{oh}$  is roughness height for surface heat transfer. When calculating  $r_{av}$ ,  $d=0.67\cdot h$  (h is vegetation height),  $z_{om}=0.1\cdot h$ , and  $z_{oh}=0.1\cdot z_{om}$ ; For  $r_{as}$ ,  $d\approx 0$  m,  $z_{om}=0.005 m$  and  $z_{oh}=0.0005 m$ . Vegetation height can be generated from in-season crop type map and accumulated growing degree day (AGDD).

For net radiation, the net radiation of soil and vegetation can be calculated as:

$$\left\{ \begin{array}{ll} R_{n,s} = & \tau_{sw} \bullet (1 - \alpha_s) \bullet R_g + exp(-k_L LAI) \bullet L_{sky} \\ & + [1 - exp(-k_L LAI)] L_v - L_s \\ R_{n,v} = & (1 - \tau_{sw}) (1 - \alpha_v) R_g + [1 - exp(-k_L LAI)] \\ & \times (L_{skv} + L_s - 2L_v)] \end{array} \right\}$$
 (8)

where;  $\alpha_s$  and  $\alpha_v$  are soil and vegetation albedo;  $R_g$  is downward shortwave solar radiation acquired from meteorological data;  $k_L$  is the extinction coefficient approximately 0.95; and  $L_{sky}$ ,  $L_v$  and  $L_s$  are longwave emissions from sky, vegetation, and soil.  $L_{sky}$  could be acquired from gridded meteorological data, and  $L_v$  and  $L_s$  are calculated from vegetation LST and emissivity.  $\tau_{sw}$  is canopy shortwave radiation transmittance, which is calculated by  $\tau_{sw}$ =exp(-k<sub>S</sub> LAI), k<sub>S</sub> is light extinction coefficient varied by vegetation type and growing stage.  $\alpha_v$  and  $\alpha_s$  are vegetation and soil albedo, which are calculated from albedo and FVC (Tang and Li, 2017).

Fig. 4(b) showed the flowchart of generating parameters of ESVEP model. Both remote sensing data and meteorological data were firstly combined to generate LST/FVC trapezoid space for each pixel, LST were then used to estimate which triangle the pixel is located in, and LE of vegetation transpiration and soil evaporation are calculated using corresponding methodology and end-members. Table 4 showed the input and output parameters for ESVEP model.

# 2.6. Random forest

The Random Forest (RF) algorithm proposed by Breiman (2001) is an ensemble machine learning method for regression and classification. Each Random Forest model contains multiple classification/regression trees. The training procedure for the RF algorithm is to construct all classification/regression trees; in this procedure, each tree is constructed from root to leaf nodes using two-third of the training samples randomly selected from training sample data set and only a part of features. Every time a split of a node is made on a feature, the Gini impurity criterion for descendent nodes is less than that of the parent node. The important metric for fit is that the sum of Gini impurity decreases for each individual variable over all trees in the classification/regression forest. "Leaf node" denotes that the node cannot be further split and all samples in the node belongs to the same class. After the construction of each tree, the remaining one-third training samples are used for testing, where the test error is referred to as "out-of-bag error". Feature importance could be estimated during the training procedure of RF, with the sum of the reduction in Gini impurity criterion. When using random forest model to predict, the prediction data set should contain the same features to training samples. For a classification prediction, the output will be mode of the classes of individual trees, whereas for a regression prediction, the output will be the average of all the individual trees. The RF algorithm have several advantages: (1) it can model complex interactions among input features; (2) it runs

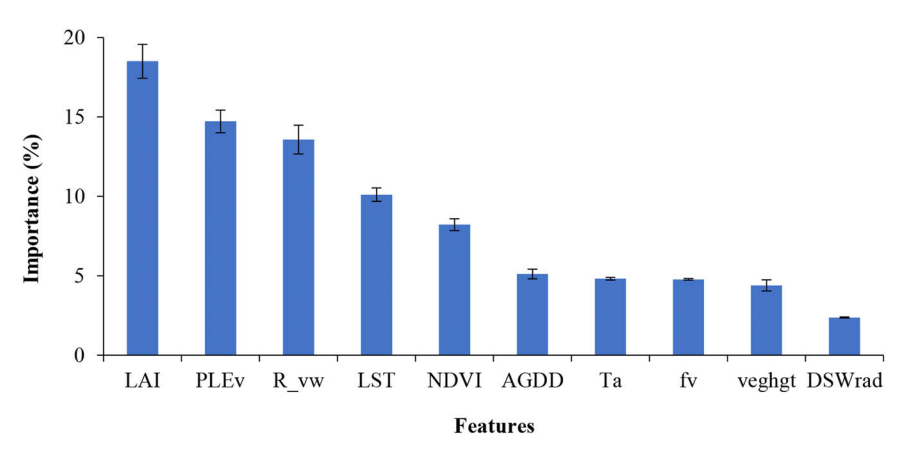


Fig. 5. The percentage feature importance of the top ten most important features. The bars denote percentage feature importance and the error line denotes standard deviation of the ten RF model runs. In this figure, the features LAI, PLEV, R\_VW, LST, NDVI, AGDD, Ta, fv, veghgt and DSWrad denote leaf area index, potential vegetation latent heat flux, canopy resistance at well-watered condition, land surface temperature, normalized difference vegetation index, accumulated growing degree day, 2-m air temperature, vegetation fraction, vegetation height and downward shortwave radiation respectively.

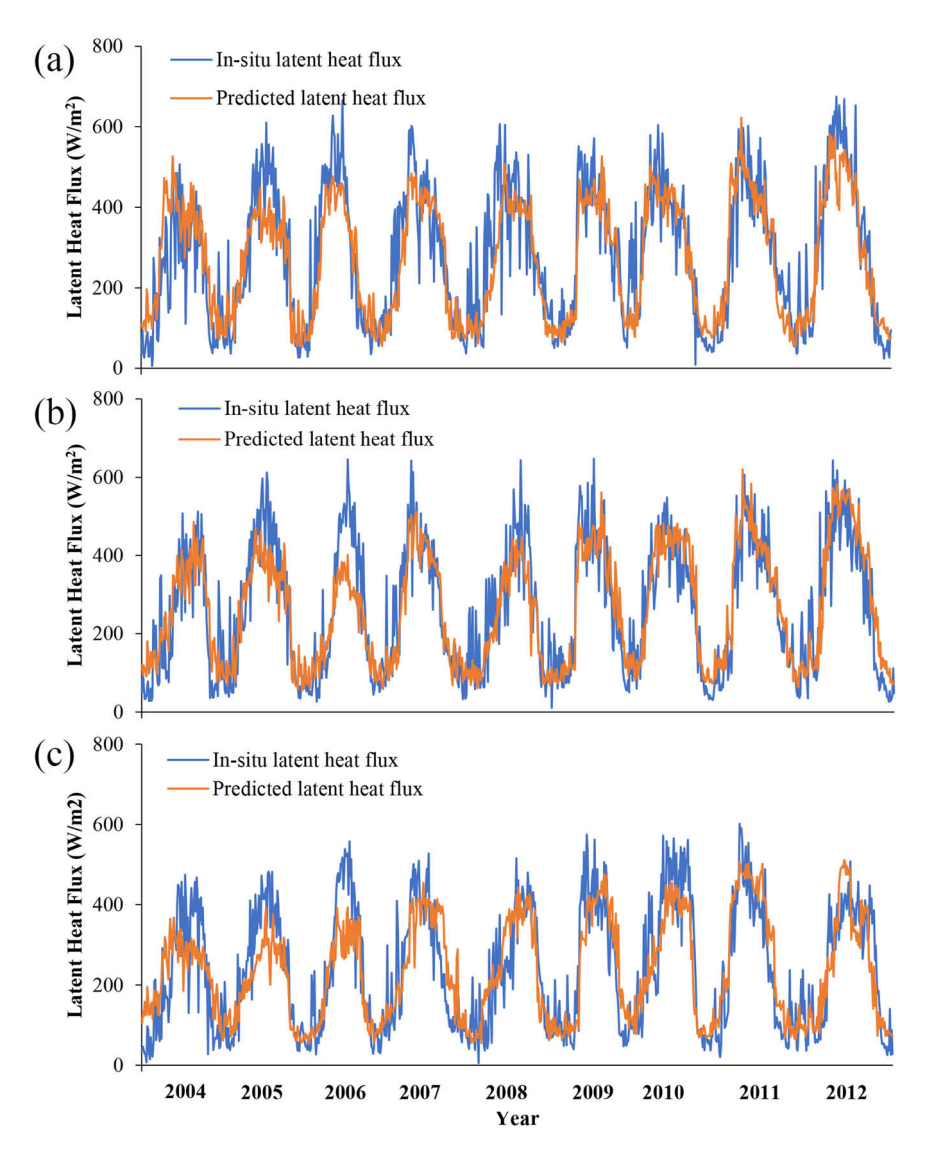


Fig. 6. Comparison of ESVEP-RF with Scenario A and in-situ LE, (a) US-NE1, (b) US-NE2, (c) US-NE3.

efficiently on large datasets and not sensitive to noise or over-fitting; and (3) it automatically uses the optimal features to construct RF model. Therefore, RF classification algorithm has been widely used in many remote sensing domains such as land cover classification and

quantitative land surface parameters regression (Belgiu and Drăguţ, 2016). In this study, the feature importance for the ET calculation are estimated using RF. All features in Table 4 are used as input features, the calculations were repeated 10 times, and the average percentage Gini

**Table 5**Yearly error parameter values of the ESVEP-RF LE for Scenario A.

Year		US-NE1				US-NE2	US-NE2			US-NE3		
	Bias (W/m²)	RMSE (W/m <sup>2</sup> )	R <sup>2</sup>	Training sample number	Bias (W/m²)	RMSE (W/m <sup>2</sup> )	R <sup>2</sup>	Training sample number	Bias (W/m²)	RMSE (W/m <sup>2</sup> )	$R^2$	Training sample number
2004	64.80	108.09	0.64	234	25.66	110.48	0.69	234	40.11	97.45	0.53	234
2005	-23.32	94.08	0.63	598	-24.40	91.99	0.73	598	-31.15	104.87	0.67	598
2006	-23.27	90.16	0.72	832	-42.73	86.62	0.73	832	-8.30	101.80	0.57	832
2007	-20.12	92.26	0.71	1244	-6.99	89.04	0.81	1244	6.98	93.04	0.72	1244
2008	-40.71	88.48	0.75	1716	-35.67	82.62	0.83	1716	6.70	85.39	0.79	1716
2009	-8.96	82.63	0.85	2166	0.50	74.63	0.81	2166	23.96	82.73	0.80	2166
2010	-6.61	78.02	0.83	2580	15.36	73.34	0.82	2580	-31.12	81.33	0.81	2580
2011	-3.05	73.50	0.84	3062	20.31	65.41	0.85	3062	35.28	69.78	0.86	3062
2012	-15.96	62.88	0.87	3555	21.34	55.47	0.89	3555	18.77	76.98	0.80	3555
All years together	-9.57	87.72	0.73		-2.43	81.97	0.75		6.77	86.14	0.69	

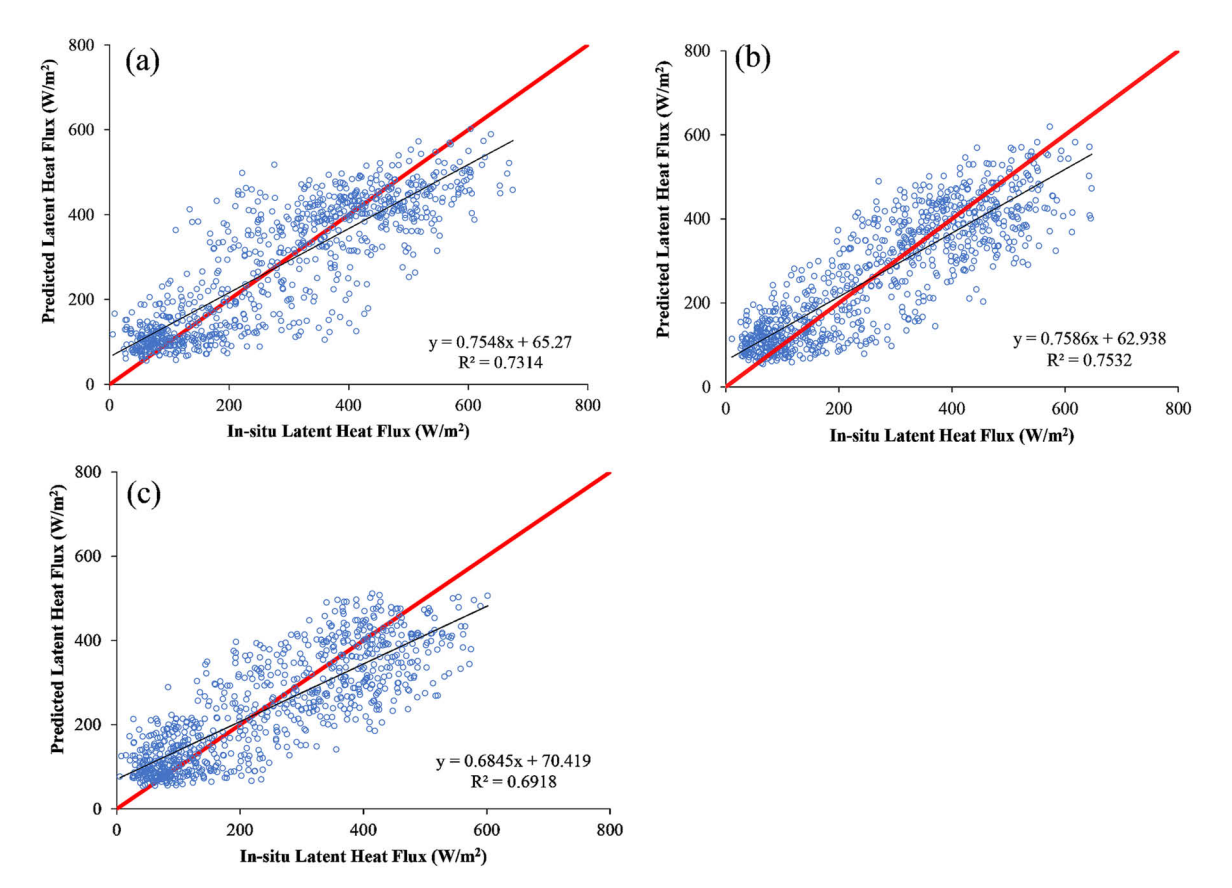


Fig. 7. Scatter plots of ESVEP-RF LE with Scenario A and in-situ LE. (a) US-NE1, (b) US-NE2, (c) US-NE3. The red lines in the figures are 1:1 lines.

score for each feature was used to generate feature importance. Next, the RF algorithm was also used for ET calculation. For each experiment, the RF model was trained with training samples. All features were included in the training procedure as RF could automatically selected the optimal features. Finally, RF models were then used to predict ET for the testing samples. The RF algorithm was implemented using the RandomForest package for R (Liaw and Wiener, 2014), the number of trees in the ensemble was set to 1000 to allow convergence of the error statistic, and the number of features to split the nodes in trees was set to the square root of the total number of input features (Loosvelt et al., 2012).

## 2.7. Accuracies evaluation metrics

We used Bias error, root mean square error (RMSE) and coefficient of determination ( $\mathbb{R}^2$ ) between the ESVEP-RF and in-situ LE. Although the ESVEP model could separate radiation and heat flux of soil part from the

vegetation part, in-situ data did not provide these data separately, so that we just verified total actual LE of ESVEP-RF. The equations used for calculating Bias, RMSE and R<sup>2</sup> are as follows:

Bias = 
$$\frac{1}{N} \sum_{1}^{N} (z_f - z_0)$$
 (9)

$$RMSE = \sqrt{\frac{\sum\limits_{1}^{N}\left(z_{f}-z_{0}\right)^{2}}{N}} \tag{10}$$

$$R^{2} = 1 - \frac{\sum (y_{i} - \widehat{y_{i}})^{2}}{\sum (y_{i} - \overline{y_{i}})^{2}}$$
(11)

where N is the size of sample size,  $(z_f-z_0)$  is the difference of each pair of in-situ and predicted LE,  $\sum (y_i-\widehat{y}_1)^2$  is the sum of residuals squared,

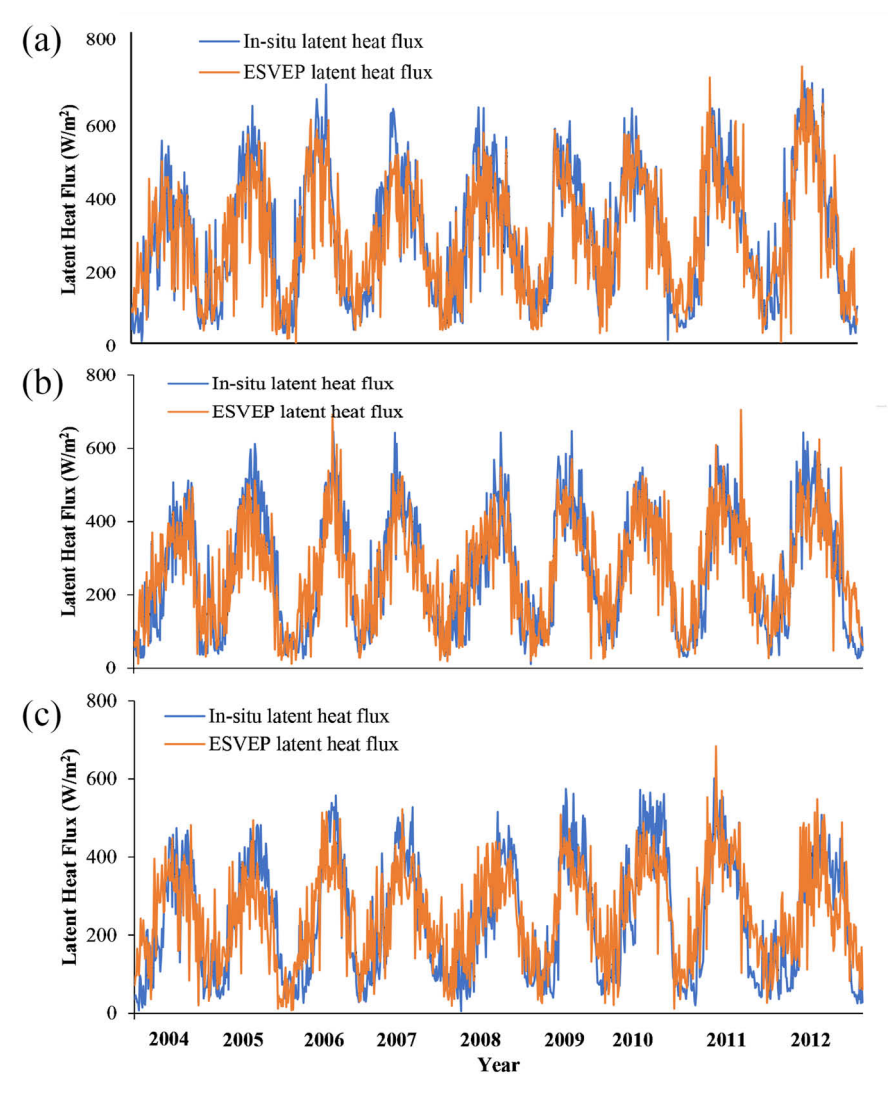


Fig. 8. Comparison of ESVEP LE and in-situ LE, (a) US-NE1, (b) US-NE2, (c) US-NE3.

**Table 6**Yearly error parameter values of the ESVEP LE.

Year		US-NE1			US-NE2			US-NE3		
	Bias (W/m <sup>2</sup> )	RMSE (W/m <sup>2</sup> )	R <sup>2</sup>	Bias (W/m <sup>2</sup> )	RMSE (W/m <sup>2</sup> )	R <sup>2</sup>	Bias (W/m <sup>2</sup> )	RMSE (W/m <sup>2</sup> )	R <sup>2</sup>	
2004	11.71	91.32	0.62	15.55	96.65	0.59	30.13	98.40	0.59	
2005	-25.02	109.26	0.59	-38.90	91.84	0.62	-31.90	91.98	0.59	
2006	-0.62	100.63	0.61	5.59	105.68	0.76	11.74	106.91	0.47	
2007	-15.51	91.08	0.71	-12.01	93.98	0.66	4.68	92.87	0.61	
2008	-26.43	100.08	0.69	2.55	106.26	0.70	18.86	103.22	0.64	
2009	-18.02	87.75	0.71	-10.62	93.61	0.65	3.95	87.95	0.62	
2010	-4.50	103.22	0.69	2.37	97.57	0.71	-19.95	94.33	0.71	
2011	5.47	93.38	0.69	16.68	84.94	0.69	41.74	92.71	0.68	
2012	-2.26	87.41	0.75	0.71	86.96	0.65	13.30	89.45	0.70	
All years together	-8.72	96.52	0.68	-2.38	95.62	0.66	8.10	97.15	0.61	

and  $\sum {(y_i - \overline{y}_l)^2}$  is the sum of the distance the data is away from the mean all squared. The ESVEP can be used to divide soil evaporation from vegetation transpiration, but the in-situ data does not provide the parameters for vegetation and soil separately, so that we only verified the total LE of the two parts together.

# 3. Results and discussion

### 3.1. Feature importance

We used all samples between 2003 and 2012 to calculate feature importance. Fig. 5 shows the top ten most important features among all features used in this study, and percentage importance sum of the top ten features was 85.57%. Among all remote sensing, meteorological and ESVEP model features, LAI was the most important feature. The average

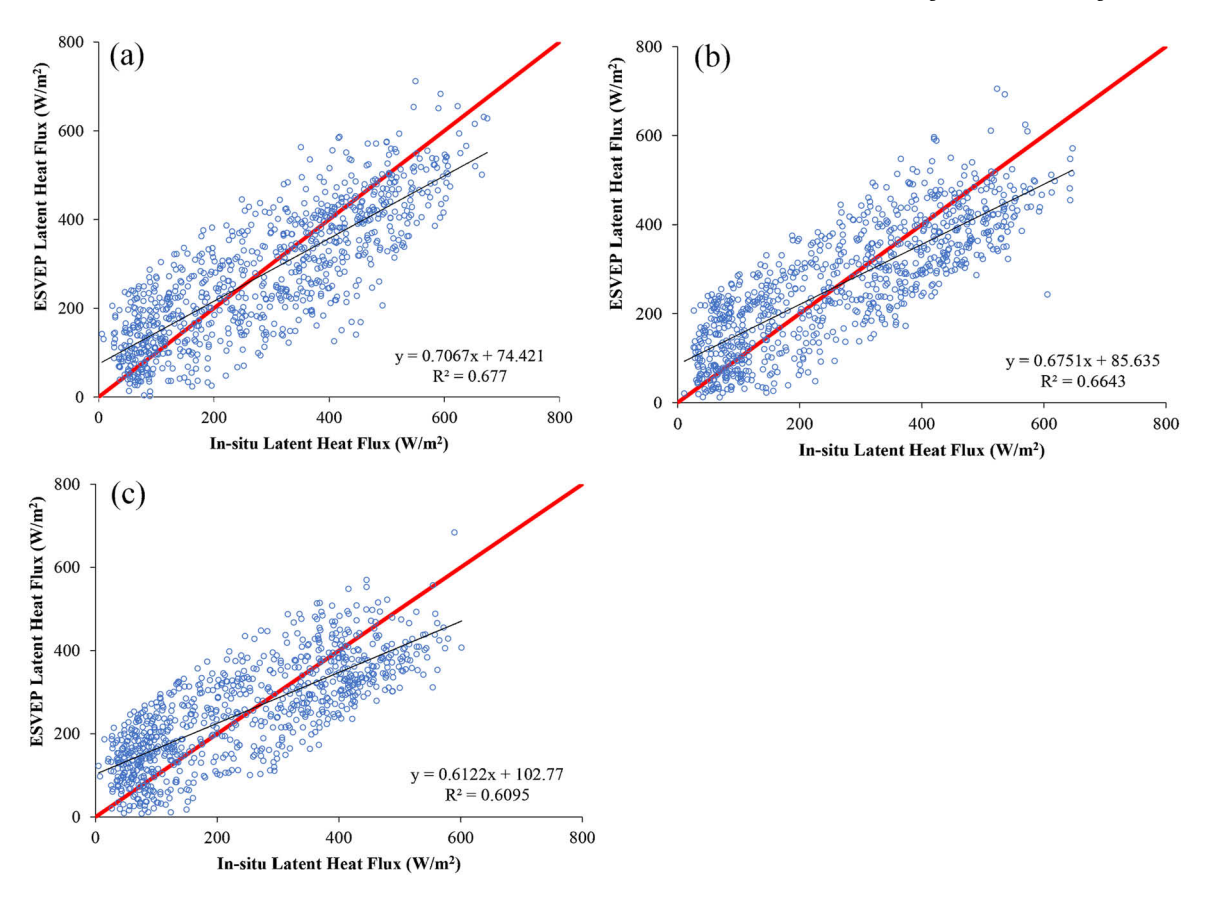


Fig. 9. Scatter plots of ESVEP LE and in-situ LE. (a) US-NE1, (b) US-NE2, (c) US-NE3. The red lines in the figures are 1:1 lines.

percentage importance of LAI for ET calculation was 18.49%, which indicated that vegetation growth was closely related to crop ET. This is because higher leaf area of the plant creates more opportunity for water vapor to leave from plant as transpiration (Monteith, 1981). In addition, higher vegetation cover means the plants absorb more solar photons and then convert more energy by transpiration (Pereira et al., 2020). Although NDVI and FVC were also proxies for the vegetation greenness condition, average percentage importance of NDVI and FVC were just 8.22% and 4.76%, respectively. This maybe because NDVI is more sensitive at low greenness time phases, and when vegetation greenness is high, NDVI is saturated and cannot describe vegetation growth precisely (Hao et al., 2020a; Wardlow et al., 2007). Furthermore, the FVC calculation is highly dependent on NDVI in this study, the NDVI saturation at high biomass level also led to the uncertainty of FVC. For other features, PLEv and R-vw had high contribution for ET calculation as the average percentage importance of the two features were 15.71% and 13.57%, respectively. PLEv and R-vw were used to describe energy balance situation when the crop was not water-stressed, and determined the potential LE of the given sample. This indicated that the samples used in this study was not under water-stress condition, which was consistent with the fact that US-NE1 and US-NE2 sites were water-sufficient as they were irrigated sites. Furthermore, LST and Ta which describe plant water status were also amongst the most important features, with an average percentage importance percentage of 10.11% and 4.81%, respectively. The other two high contribution features are AGDD and Veghgt, which are used to describe crop growth stage.

### 3.2. Latent heat flux validation using in-situ measurements

We first generated LE using ESVEP-RF with training samples of the previous years from all three NE sites, and then compared ESVEP-RF LE with in-situ LE measurement. Fig. 6 showed that ESVEP-RF LE had high

uncertainty before 2008, with yearly RMSE were higher than 80 W/m<sup>2</sup> and R<sup>2</sup> were lower than 0.8 in the most cases (Table 5). The reason for high uncertainty was that the number of training samples was low. It is notable that LE prediction accuracies increased with training sample number (Table 5). For example, when we only acquired 234 training samples from all three NE sites in 2003, the yearly RMSE of US-NE1, US-NE2 and US-NE3 were 108.09 W/m<sup>2</sup>, 110.48 W/m<sup>2</sup> and 97.45 W/m<sup>2</sup> in 2004, and the yearly R<sup>2</sup> of the three sites were 0.64, 0.69 and 0.53, respectively. However, when we calculated LE in 2011, we used all samples between 2003 and 2010, with a total of 3062 samples acquired. The yearly RMSE of ESVEP-RF LE for US-NE1, US-NE2 and US-NE3 were  $73.50 \text{ W/m}^2$ , 65.41 W/m<sup>2</sup> and 69.78 W/m<sup>2</sup>, and yearly R<sup>2</sup> of the three sites were 0.84, 0.85 and 0.86 respectively. Table 5 also showed that when the number of training samples was more than 3000, RMSE and R<sup>2</sup> remained stable, which indicated that 3000 training samples could be sufficient for training RF models. ESVEP result for site US-NE1 in 2012 was not accurate since the LE in 2012 was higher than all the training samples we have collected between 2003 and 2011, indicating that when LE status of the given pixel is not included in the training samples sets, ESVEP-RF may not calculate LE accurately. Finally, when considering all samples between 2003 and 2012, R<sup>2</sup> for the three sites were 0.73, 0.75 and 0.69 (Fig. 7 and Table 5).

To further compare LE derived from ESVEP model and ESVEP-RF, we also used the ESVEP model to calculate LE between 2003 and 2012 (Fig. 8), and found that LE calculated from the ESVEP model was not as accurate as the calculation from ESVEP-RF. In addition, when training samples are sufficient, ESVEP-RF outperformed ESVEP model LE. For example, in 2012, the RMSE and  $R^2$  of ESVEP LE were 87.41 W/ $m^2$  and 0.75 for US-NE1 (Table 6); and RMSE and  $R^2$  of ESVEP-RF LE for US-NE1 were 62.88 W/ $m^2$  and 0.87 and (Table 5). We then collected all samples between 2004 and 2012, LE derived from ESVEP-RF also had lower RMSE and higher  $R^2$  than ESVEP model LE for all three sites (Table 6),

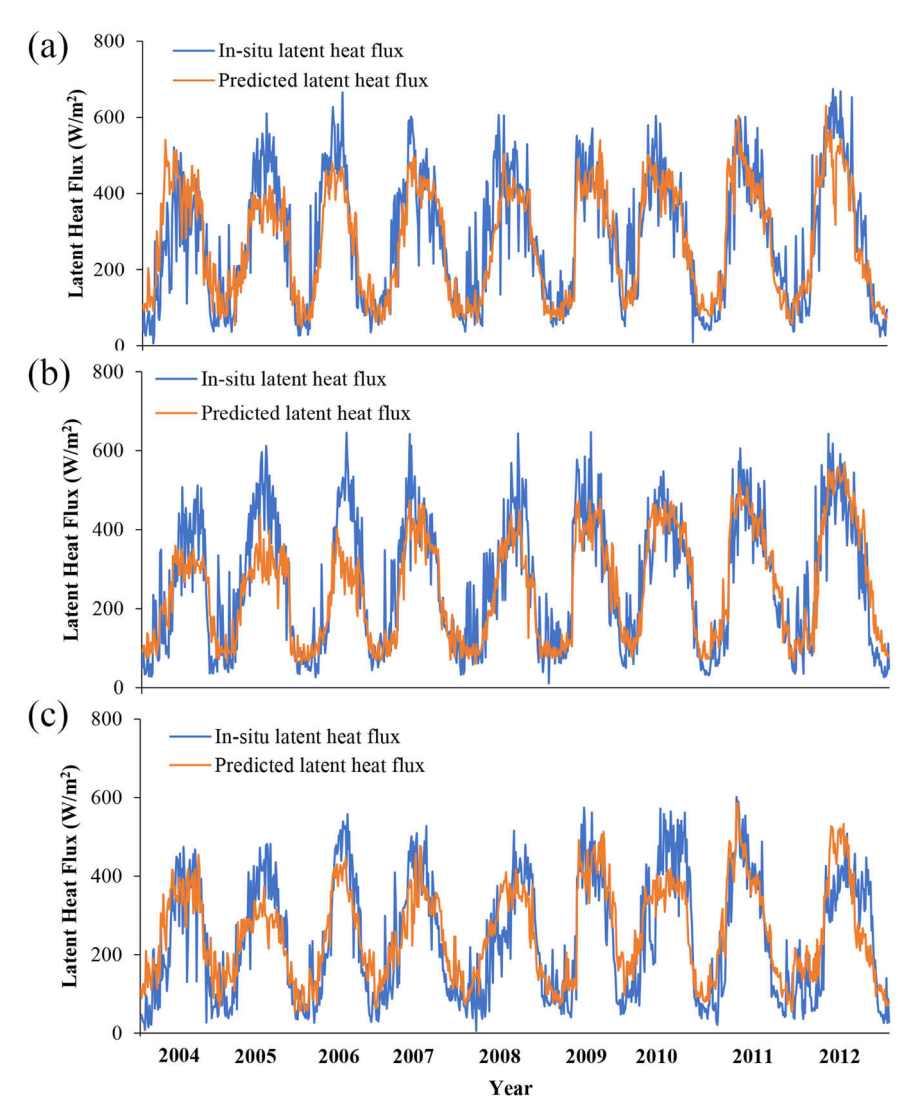


Fig. 10. Comparison of ESVEP-RF with Scenario B and in-situ LE, (a) US-NE1, (b) US-NE2, (c) US-NE3.

**Table 7**Yearly error parameter values of the ESVEP-RF LE for Scenario B.

Year		US-NE1			US-NE2				US-NE3			
	Bias (W/m²)	RMSE (W/m <sup>2</sup> )	R <sup>2</sup>	Training sample number	Bias (W/m²)	RMSE (W/m <sup>2</sup> )	$R^2$	Training sample number	Bias (W/ m <sup>2</sup> )	RMSE (W/m <sup>2</sup> )	R <sup>2</sup>	Training sample number
2004	67.86	111.84	0.62	175	-4.39	94.07	0.66	155	46.44	105.67	0.69	154
2005	-9.58	91.23	0.61	429	-58.04	114.96	0.69	407	-17.63	90.98	0.55	395
2006	-1.26	82.03	0.72	584	-56.76	124.74	0.68	522	-0.09	80.64	0.71	558
2007	-14.61	86.22	0.82	848	-23.01	95.84	0.71	795	7.28	83.16	0.80	845
2008	-34.72	103.79	0.72	1158	-42.52	82.31	0.79	1106	17.44	101.82	0.76	1168
2009	-8.33	84.35	0.80	1432	-15.73	80.94	0.86	1415	30.72	75.50	0.70	1485
2010	-4.72	74.97	0.73	1706	7.18	70.09	0.80	1681	-22.04	84.25	0.79	1773
2011	-2.04	74.48	0.81	2032	13.58	75.57	0.79	2017	27.64	74.14	0.81	2075
2012	-19.16	70.47	0.81	2351	18.30	58.43	0.88	2347	24.69	80.87	0.75	2412
All years together	-4.23	90.16	0.7172		-17.10	90.10	0.7123		12.56	89.26	0.6768	

and the bias estimation results of ESVEP LE and ESVEP-RF LE are similar. The fitted lines of the calculated LE and in-situ LE showed that ESVEP-RF LE were closer to 1:1 line as the fitted lines of ESVEP-RF LE and in-situ LE had higher slope and lower intercept (Figs. 7 and 9).

Although we have used independent training and test samples to estimate the potential of ESVEP-RF of ET calculation, the generalizability of RF models trained from training samples in other regions is not

clear. Therefore, we used training and test samples from different sites to test the generalizability of RF models (Scenario B). Similar to the ESVEP-RF calculation results with training samples from all three sites, LE calculation accuracies were low with high bias and RMSE when number of training samples was not sufficient (Fig. 10). Although LE calculated in Scenario B were not so accurate as the LE generated in Scenario A, the accuracies were still acceptable when the training sample number was

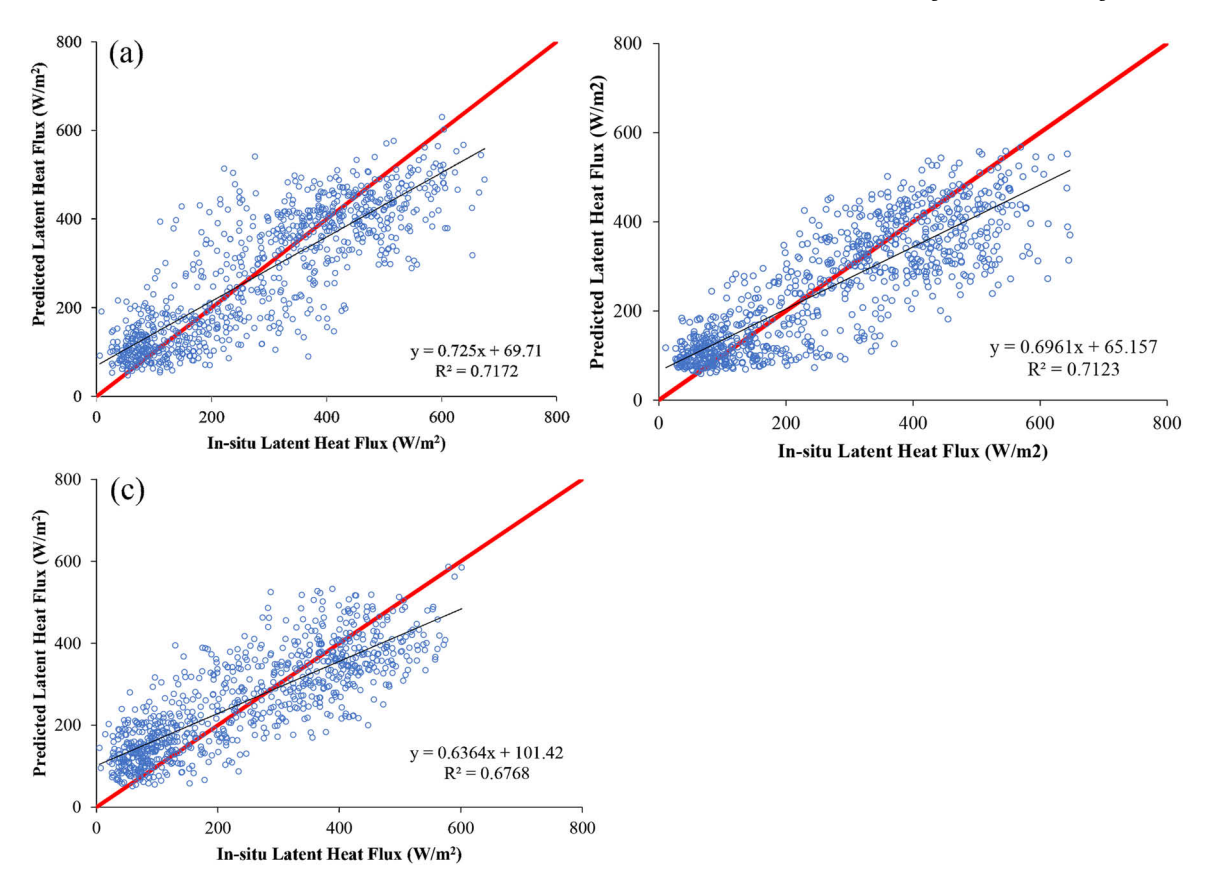


Fig. 11. Scatter plots of ESVEP-RF LE with Scenario B and in-situ LE. (a) US-NE1, (b) US-NE2, (c) US-NE3. The red lines in the figures are 1:1 lines.

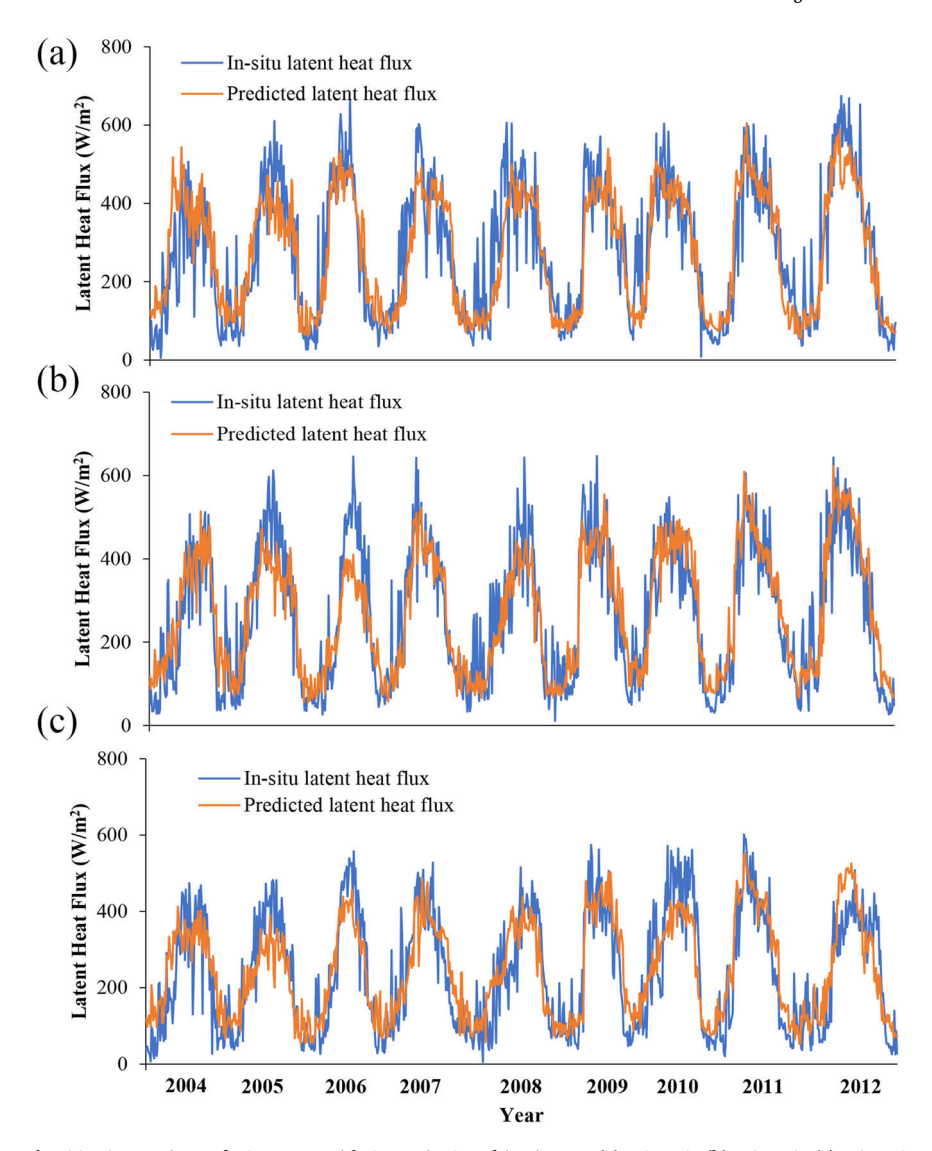
sufficient. For example, when training samples were collected from US-NE2 and US-NE3 between 2003 and 2011, RMSE and R<sup>2</sup> of US-NE1 in 2012 were 70.41 W/m<sup>2</sup> and 0.81 (Table 7), which showed that the LE could be accurately calculated even although samples of test site were not used during the training procedure. We further compared the LE of Scenario B calculated among the three sites, and found that accuracies of US-NE1 and US-NE2 were better than US-NE3 with higher yearly R<sup>2</sup> and lower RMSE (Table 7). For example, in year 2012, R<sup>2</sup> of ESVEP-RF and in-situ LE for US-NE1 and US-NE2 were higher than 0.8, but R2 for US-NE3 was only around 0.74. When considering samples of all nine years (between 2004 and 2012), fitted lines of the LE calculated from the ESVEP-RF with Scenario B were not close to 1:1 lines as the fitted lines of LE calculated from ESVEP-RF with Scenario A, as shown in Fig. 11 (c), slope and bias of the fitted line were 0.64 and 101.42 W/m<sup>2</sup>, respectively. Furthermore, LE calculated for US-NE3 had the lowest accuracy among the three sites. The relatively low accuracies of US-NE3 LE with Scenario B was probably because the sites US-NE1 and US-NE2 are irrigation sites, but US-NE3 was a rainfed site. When calculating LE for US-NE1, the training samples of NE2 which was also an irrigation site were also used, but when calculating LE of US-NE3 (a rainfed site), all training samples were collected from irrigation sites, and an RF model trained on irrigation sites might not be used to calculate the LE of a rainfed site accurately.

To further test whether the relatively low LE calculation accuracies of US-NE3 was caused by the mismatch between training and test samples, we divided the training set into rainfed and irrigation (Scenario C), and then generated RF model for irrigation and rainfed samples separately. Compared with Scenario A and Scenario B, the LE predicted in Scenario C were more consistent with in-situ LE (Fig. 12). Table 8 also showed that for all three NE sites, RMSE of Scenario C were lower than the other two scenarios in 2010, 2011 and 2012 when the number of training samples were sufficient; as a result, R<sup>2</sup> of Scenario C were also higher. For example, RMSE and R<sup>2</sup> of US-NE3 for Scenario C were

74.83 W/m² and 0.82 in 2010, which were significantly better than those for Scenario A (in Table 5, 81.33 W/m² and 0.81) and B (in Table 7, 84.25 W/m² and 0.78). When considering all the samples together, scatter plots (Fig. 13) also showed that the fitted lines of Scenario C were closer to 1:1 lines, the bias of fitted lines for US-NE3 was around 80 W/m² (Fig. 13c), which was more than 20 W/m² lower than that of Scenario B (Fig. 11c). This result indicated that when training samples and test samples were for the same irrigation, the performance of ESVEP-RF model improved, which was consistent with the relatively low accuracies of Scenario B.

### 3.3. Applicability of ESVEP-RF in 2018 and 2019

To further test the applicability of the ESVEP-RF, we used all samples collected between 2003 and 2012 to train the RF models and calculated LE in 2018 and 2019, training samples collected from US-NE1 and US-NE2 were used to calculate LE for US-NE1, US-NE2, US-KL1 and US-KM1 and training samples collected from US-NE3 were used to calculate LE for US-NE3. Fig. 14 showed that LE calculated from ESVEP-RF had good consistency with in-situ data and described the yearly LE trend in both NE and MI sites. The scatter plots (Fig. 15) also showed that for the three NE sites, ESVEP-RF LE and in-situ LE had good linear correlation as the R<sup>2</sup> of the three sites were between 0.8 and 0.85, and RMSE were between 55 W/m<sup>2</sup> and 65 W/m<sup>2</sup> in the most cases. Furthermore, the LE calculation accuracies of the two MI sites were slightly worse than the three NE sites, the R2 of US-KL1 and US-KM1 were 0.76 and 0.74, and the RMSE were 69.34 W/m<sup>2</sup> and 71.69 W/ m<sup>2</sup>, respectively. The uncertainty of the LE calculated from ESVEP-RF was mainly caused by the LE overestimation at the low LE time phases (mainly around DOY 101-130 and 260-300), when the in-situ LE was lower than 100 W/m<sup>2</sup>, and the yearly bias of the ESVEP-RF LE ranged from 20 W/m<sup>2</sup> to 40 W/m<sup>2</sup> (Fig. 15). It is notable that no training samples were collected for the sites US-KL1 and US-KM1, this indicated



 $\textbf{Fig. 12.} \ \ \textbf{Comparison of ESVEP-RF with Scenario C and in-situ LE, (a) US-NE1, (b) US-NE2, (c) US-NE3.}$ 

**Table 8**Yearly error parameter values of the ESVEP-RF LE for Scenario C.

Year	Bias (W/ m²)	US-NE1				US-NE2	US-NE2			US-NE3		
		RMSE (W/m <sup>2</sup> )	$R^2$	Training sample number	Bias (W/m²)	RMSE (W/m <sup>2</sup> )	R <sup>2</sup>	Training sample number	Bias (W/m²)	RMSE (W/m <sup>2</sup> )	R <sup>2</sup>	Training sample number
2004	76.65	124.81	0.65	154	35.44	88.36	0.71	154	17.73	95.42	0.63	80
2005	-25.97	94.86	0.56	395	-17.78	88.93	0.73	395	-45.52	92.47	0.67	203
2006	-26.79	91.96	0.74	558	-31.56	102.70	0.74\	558	-45.21	87.60	0.68	274
2007	-16.28	77.32	0.80	845	-4.08	84.65	0.82	845	13.58	80.28	0.76	399
2008	-41.83	101.97	0.78	1168	-31.14	79.30	0.84	1168	0.11	79.08	0.82	548
2009	-5.59	80.50	0.85	1485	11.99	77.20	0.83	1485	3.02	81.57	0.76	681
2010	-1.84	72.30	0.74	1773	19.70	76.89	0.81	1773	-36.01	74.83	0.82	807
2011	-3.45	68.92	0.83	2075	23.98	62.98	0.77	2075	34.34	69.85	0.87	987
2012	-19.13	62.18	0.88	2412	21.38	56.75	0.90	2412	-4.33	70.53	0.82	1143
All years together	-8.24	87.34	0.7355		3.28	80.33	0.7633		-6.16	81.82	0.7234	

that the ESVEP-RF model trained with from Nebraska sites had the potential to be used in other regions with similar cropland, particularly in the Corn Belt.

### 3.4. Advantages and limitations

In this study, we proposed a practical workflow using the output of the ESVEP model as input features in RF model for ET calculation. The advantage of the ESVEP model is that the model divides soil evaporation from vegetation transpiration, and then provides more parameters

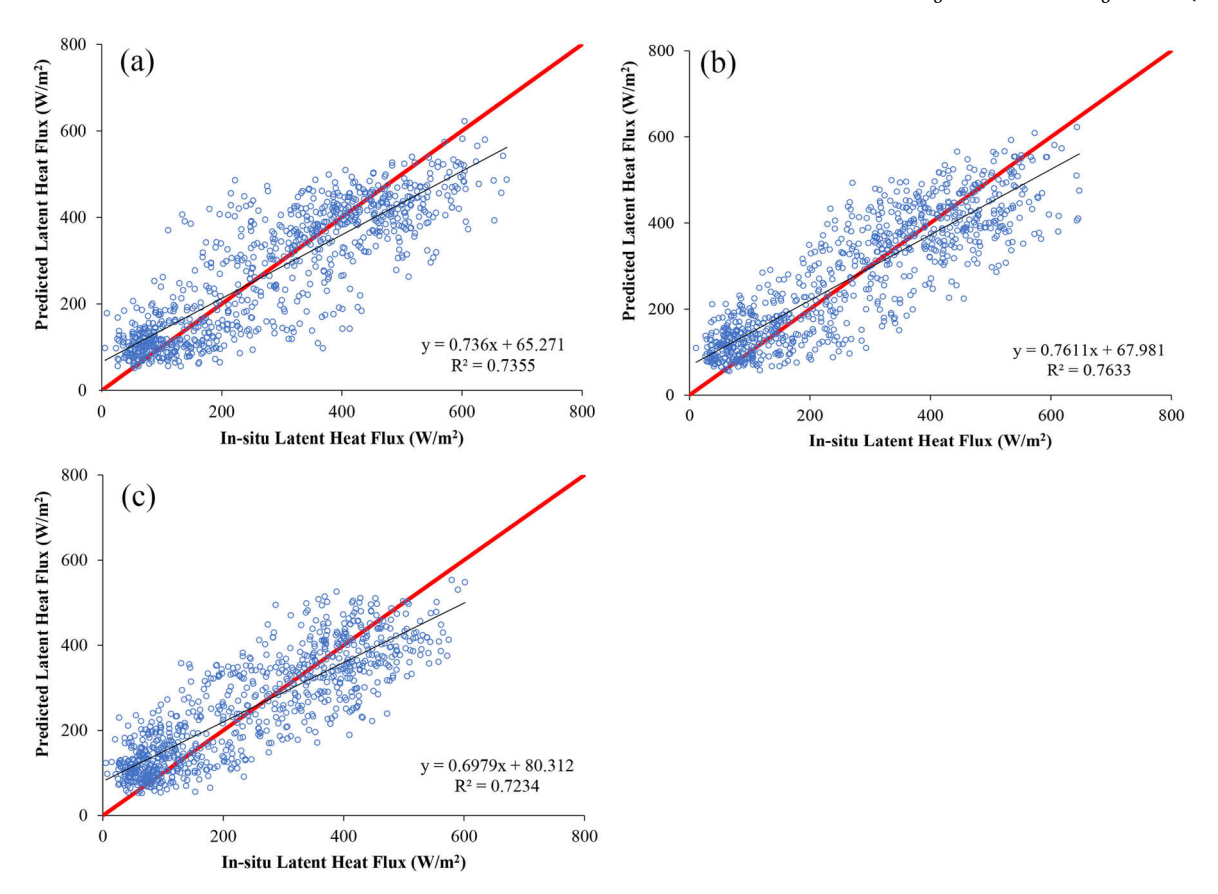


Fig. 13. Scatter plots of ESVEP-RF LE with Scenario C and in-situ LE. (a) US-NE1, (b) US-NE2, (c) US-NE3. The red lines in the figures are 1:1 lines.

which could describe the energy balance more precisely. The limitation of the original ESVEP model is that only a linear method is used to calculate the correlation between the LE of the given pixel and the two triangles in the LST/FVC space (Fig. 4), so that we use RF regression to improve the drawback of the original ESVEP model because RF regression has shown potential for describing nonlinear correlation. From the perspective of RF, most existing studies only use features which are available from the remote sensing land surface products, such as NDVI, LAI and PAR.etc (Carter and Liang, 2019; Chia et al., 2020; Filgueiras et al., 2020), but no parameters generated from the LST-based physical models are considered, this study showed that some ESVEP model derived parameters (such as PLEv and R-vw) are selected as high-importance features, which indicates the contribution of ESVEP model for the ESVEP-RF model.

However, there are still some drawbacks of the ESVEP-RF workflow. The most important issue for the ESVEP-RF method is collecting training sample as the final procedure of the ET calculation is based on machine learning algorithms. Our results have shown that training sample data size affect the ESVEP-RF calculation accuracies, which is consistent with Carter and Liang (2019) that small training samples size cannot calculate LE accurately. Another issue related to the training samples collection is the representative of the training samples set. Dou and Yang (2018) found that the same training data set have different performance for multiple ecosystems type, which is similar to the Scenario B results in this study as the RF models trained by samples of irrigation field samples cannot be used to calculate the LE of rainfed fields accurately. Therefore, the study region should be carefully cataloged based on the characters of the land cover, and training samples need to be selected with large quantity and cover each catalog to ensure both the sample set size and representative.

Another limitation of ESVEP-RF is that the ESVEP model needs crop type and planting date as inputs to calculate several parameters, such as AGDD, height and aerodynamic resistance. However, gridded up-to-date

crop type and planting information are not available for practical ET monitoring. For crop type data, existing crop type maps, such as CDL data, are not available before the crop harvest (Boryan et al., 2011), and the accurate early-season crop type map are not available before July (Hao et al., 2020a; Hao et al., 2015). Although the predicted crop type maps can be generated before the start of the growing season (Zhang et al., 2019), this data contain large uncertainties that may seriously affect the LE calculation accuracy. For planting date information, although suggested planting dates are provided (Shroyer et al., 1996), the gridded actual planting date information of the target year is still not available before growing season begins. Therefore, a practical solution is to collect the crop type and planting data information from the farmers' report, but this would limit the up-to-date application of ESVEP-RF to certain fields with all necessary input information.

## 4. Conclusion

This present paper proposed a new workflow for ET calculation by combining the advantages of ESVEP model and RF. Remote sensing and meteorological data were used as inputs for the ESVEP-RF method, which was tested using all available in-situ data from five flux tower sites of 12 years (2003–2012, 2018 and 2019). The main conclusions are as follows:

- (1) ESVEP-RF showed good potential for calculating ET when the number of training samples is sufficient and representative. In 2010 and 2011,  $R^2$  of LE calculated by ESVEP-RF were around 0.8 and RMSE were around 70 W/m², which outperformed the original ESVEP model. The uncertainty in ESVEP-RF is mainly caused by the overestimation of LE at low LE level time phases.
- (2) Among all remote sensing, meteorological and ESVEP model output features, LAI was selected as the most important feature as the percentage importance of LAI calculated from RF was

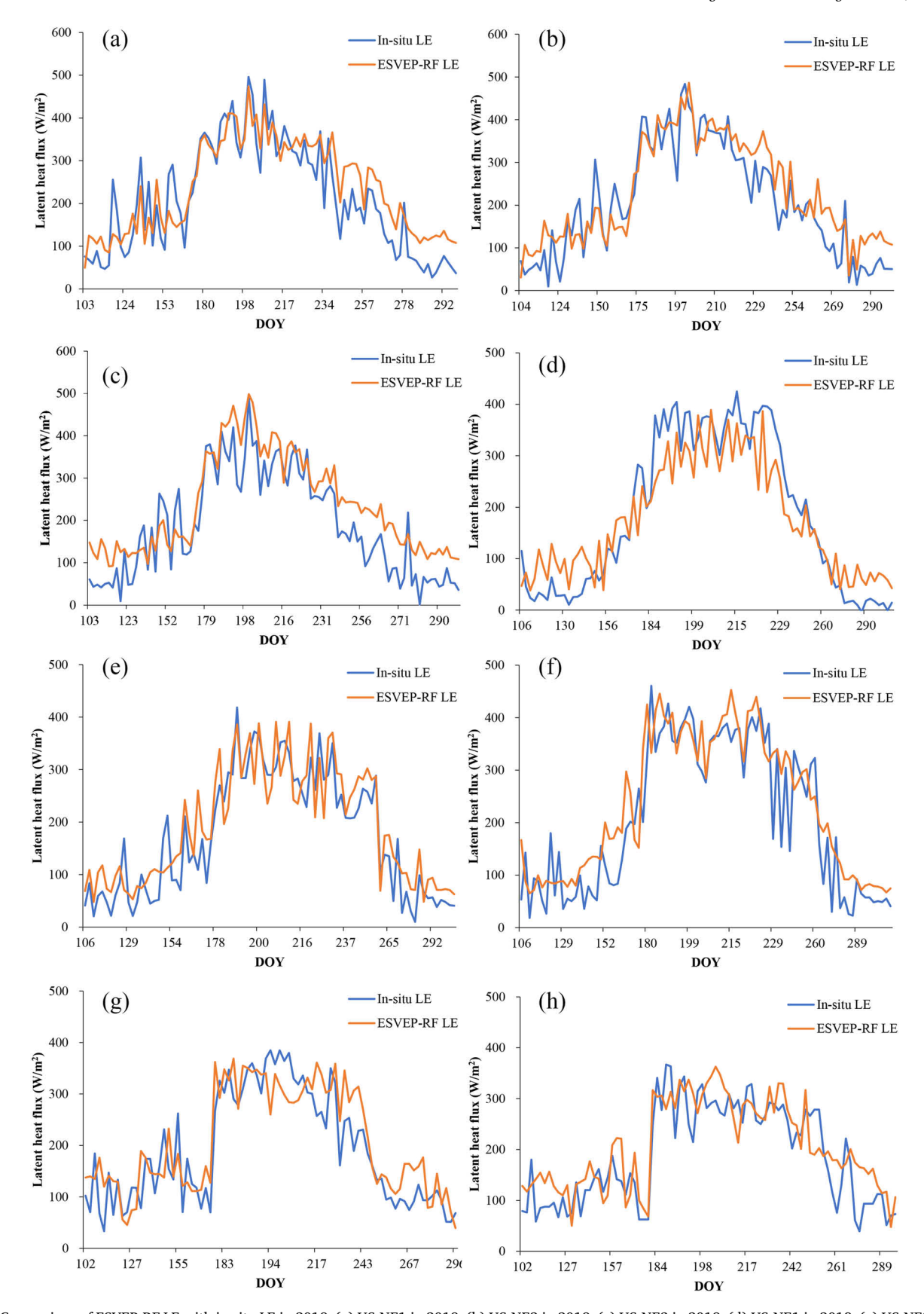


Fig. 14. Comparison of ESVEP-RF LE with in-situ LE in 2019, (a) US-NE1 in 2019, (b) US-NE2 in 2019, (c) US-NE3 in 2019, (d) US-NE1 in 2018, (e) US-NE2 in 2018, (f) US-NE3 in 2018, (g) US-KL1 in 2018, (h) US\_KM1 in 2018. In this figure, DOY denotes day of year.

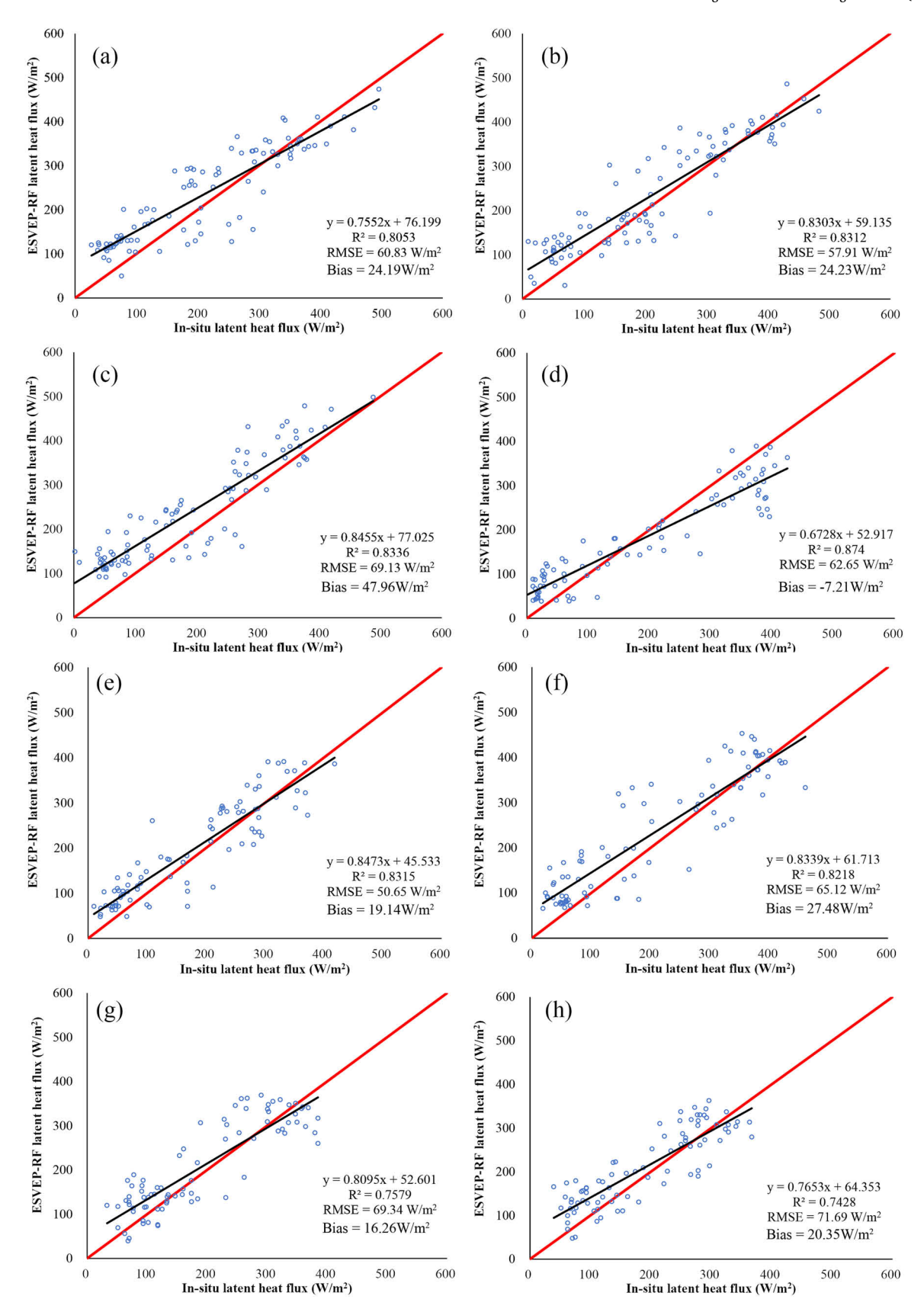


Fig. 15. Scatter plots of ESVEP-RF LE in-situ LE in 2019. (a) US-NE1 in 2019, (b) US-NE2 in 2019, (c) US-NE3 in 2019, (d) US-NE1 in 2018, (e) US-NE2 in 2018, (f) US-NE3 in 2018, (g) US-KL1 in 2018, (h) US\_KM1 in 2018. The red lines in the figures are 1:1 lines.

- 18.49%. In addition, the percentage importance of PLEv and R-vw were 15.71% and 13.57%, respectively. These parameters were used to describe vegetation transpiration in case that the plant is non-water-stressed.
- (3) ESVEP-RF had good extendibility as the method achieved R<sup>2</sup> higher than 0.7 when training and validation samples were from independent sites. In addition, the ESVEP-RF model generated from samples between 2003 and 2012 achieved good accuracy for LE calculation in 2018 and 2019, RMSE were between 55 W/m<sup>2</sup> and 70 W/m<sup>2</sup> and R<sup>2</sup> were around 0.8 for the five test sites.

As ESVEP-RF driven by 2003–2012 training samples showed good potential for calculating ET in 2018 and 2019, we have used the method to calculate grided instantaneous LE of satellite overpass time under cloud-free condition with predicted crop type map and suggested planting date information as input, this LE data are then used to generate cloud-free condition daily ET, which is a part of the all-weather up-to-date ET data product in NE, the product is accessible at Watersmart Data Information Portal as "machine learning ET" (https://geobrain.csiss.gmu.edu/watersmartport/web/). As the limitations of training samples and input information affect the accuracy of ESVEP-RF seriously, more attention should be paid to ensure the sample size and representative as well as the early-season crop type and planting data information when applying the ESVEP-RF to generate up-to-date LE data.

### **Declaration of Competing Interest**

The authors declare that they have no known competing financial interests or personal relationships that could have appeared to influence the work reported in this paper.

### Acknowledgments

The MODIS and NLDAS-2 data were acquired by the National Aeronautics and Space Administration (NASA), the NWM data were acquired by the Office of Water Prediction (OWP) and the in-situ data were acquired by FLUXNET and AmeriFlux. This research is supported by a grant from the NSF INFEWS program (grant #: CNS-1739705, PI: Prof. Liping Di). The authors would like to thank Ms. Julia Di of Stanford University for editing and proofreading this manuscript.

### References

- Allen, R., Tasumi, M., Trezza, R., 2007. Satellite-based energy balance for mapping evapotranspiration with internalized calibration (METRIC) – model. J. Irrig. Drain. Eng. 133, 133–394.
- Anderson, M.C., Norman, J.M., Mecikalski, J.R., Otkin, J.A., Kustas, W.P., 2007.
  A climatological study of evapotranspiration and moisture stress across the continental United States based on thermal remote sensing: 2. Surface moisture climatology. J. Geophys. Res.: Atmos. 112, 112.
- Belgiu, M., Drăguţ, L., 2016. Random forest in remote sensing: a review of applications and future directions. ISPRS J. Photogramm. Remote Sens. 114, 24–31.
- Boryan, C., Yang, Z.W., Mueller, R., Craig, M., 2011. Monitoring US agriculture: the US Department of Agriculture, National Agricultural Statistics Service, Cropland Data Layer Program. Geocarto Int. 26, 341–358.
- Breiman, L., 2001. Random forests. Mach. Learn. 45, 5-32.
- Burt, C., Mutziger, A.J., Allen, R., Howell, T., 2005. Evaporation research: review and interpretation. J. Irrig. Drain. Eng. 131, 131–158.
- Carlson, T.N., 2007. An overview of the "Triangle Method" for estimating surface evapotranspiration and soil moisture from satellite imagery. Sensors 7, 7-1629.
- Carter, C., Liang, S., 2019. Evaluation of ten machine learning methods for estimating terrestrial evapotranspiration from remote sensing. Int. J. Appl. Earth Obs. Geoinf. 78, 86–92.
- Chia, M.Y., Huang, Y.F., Koo, C.H., Fung, K.F., 2020. Recent advances in evapotranspiration estimation using artificial intelligence approaches with a focus on hybridization techniques—a review. Agronomy 10, 101.
- Dhungel, R., Allen, R.G., Trezza, R., Robison, C.W., 2016. Evapotranspiration between satellite overpasses: methodology and case study in agricultural dominant semi-arid areas. Meteorol. Appl. 23, 714–730.
- Di, L., 1991. Regional-Scale Soil Moisture Monitoring using NOAA/AVHRR Data. The University of Nebraska Lincoln, Ann Arbor, p. 415.

- Dou, X., Yang, Y., 2018. Evapotranspiration estimation using four different machine learning approaches in different terrestrial ecosystems. Comput. Electron. Agric. 148, 95–106.
- Farahani, H., Howell, T., Shuttleworth, W., Bausch, W.C., 2007. Evapotranspiration: progress in measurement and modeling in agriculture. Trans. ASABE 50, 50–1638.
- Filgueiras, R., Almeida, T.S., Mantovani, E.C., Dias, S.H.B., Fernandes, E.I., da Cunha, F. F., Venancio, L.P., 2020. Soil water content and actual evapotranspiration predictions using regression algorithms and remote sensing data. Agric. Water Manag. 241, 241
- Hao, P.-y, Tang, H.-j, Chen, Z.-x, Meng, Q.-y, Kang, Y.-p, 2020a. Early-season crop type mapping using 30-m reference time series. J. Integr. Agric. 19, 1897–1911.
- Hao, P., Di, L., Zhang, C., Guo, L., 2020b. Transfer Learning for Crop classification with Cropland Data Layer data (CDL) as training samples. Sci. Total Environ. 733, 138869.
- Hao, P.Y., Zhan, Y.L., Wang, L., Niu, Z., Shakir, M., 2015. Feature selection of time series MODIS data for early crop classification using random forest: a case study in Kansas, USA. Remote Sens. 7, 5347–5369.
- Jéffersonde, dO.C., Jefferson, J., Wagner, W., Niclene, O., Rafaella, O., Nathalia, R., Rubens, C., Tonny, S., Edna, B.-S., Alessana, S., 2020. Spatial variability quantification of maize water consumption based on Google EEflux tool. Agric. Water Manag. 232, 106037.
- Jiang, C., Guan, K., Pan, M., Ryu, Y., Peng, B., Wang, S., 2020. BESS-STAIR: a framework to estimate daily, 30 m, and all-weather crop evapotranspiration using multi-source satellite data for the US Corn Belt. Hydrol. Earth Syst. Sci. 24, 1251–1273.
- Jiang, L., Islam, S., Jutla, A., Ramsay, B., Eltahir, E., 2009. A satellite-based Daily Actual Evapotranspiration estimation algorithm over South Florida. Glob. PLANET. Chang. - Glob. PLANET Chang. 67, 62–77.
- Jiang, Y., Tang, R., Jiang, X., Li, Z.-L., Gao, C., 2019. Estimation of soil evaporation and vegetation transpiration using two trapezoidal models from MODIS data. J. Geophys. Res.: Atmos. 124, 7647–7664.
- Kimball, J., Running, S., 2016. A review of remote sensing based actual evapotranspiration estimation: a review of remote sensing evapotranspiration. Wiley Interdiscip. Rev.: Water 3, 834–853.
- Knipper, K.R., Kustas, W.P., Anderson, M.C., Nieto, H., Alfieri, J.G., Prueger, J.H., Hain, C.R., Gao, F., McKee, L.G., Alsina, M.M., Sanchez, L., 2020. Using highspatiotemporal thermal satellite ET retrievals to monitor water use over California vineyards of different climate, vine variety and trellis design. Agric. Water Manag. 241, 106361.
- Leng, P., Li, Z.L., Duan, S.B., Tang, R.L., Gao, M.F., 2017. A method for deriving all-sky evapotranspiration from the synergistic use of remotely sensed images and meteorological data. J. Geophys. Res. -Atmos. 122, 13263–13277.
- Li, Z.-L., Tang, R., Wan, Z., bi, Y., Zhou, C., Tang, B., Yan, G., Zhang, X., 2009. A review of current methodologies for regional evapotranspiration estimation from remotely sensed data. Sens. (Basel, Switz.) 9, 3801–3853.
- Liang, S., 2001. Narrowband to broadband conversions of land surface albedo I: algorithms. Remote Sens. Environ. 76, 213–238.
- Liang, S., 2004. Estimation of surface radiation budget: I. Broadband Albedo, quantitative remote sensing of land. Surfaces 310-344.
- Liaw, A., Wiener, M., 2014, RandomForest: Breiman and Cutler's random forests for classification and regression.
- Liu, X., Xu, J., Zhou, X., Wang, W., Yang, S., 2019. Evaporative fraction and its application in estimating daily evapotranspiration of water-saving irrigated rice field. J. Hydrol. 584, 124317.
- Long, D., Singh, V.P., 2012. A two-source trapezoid model for evapotranspiration (TTME) from satellite imagery. Remote Sens. Environ. 121, 370–388.
- Loosvelt, L., Peters, J., Skriver, H., Lievens, H., Van Coillie, F.M.B., De Baets, B., Verhoest, N.E.C., 2012. Random Forests as a tool for estimating uncertainty at pixellevel in SAR image classification. Int. J. Appl. Earth Obs. Geoinf. 19, 173–184.
- Loozen, Y., Rebel, K.T., de Jong, S.M., Lu, M., Ollinger, S.V., Wassen, M.J., Karssenberg, D., 2020. Mapping canopy nitrogen in European forests using remote sensing and environmental variables with the random forests method. Remote Sens. Environ. 247, 247
- Monteith, J.L., 1981. Evaporation and surface temperature. Q. J. R. Meteorol. Soc. 107, 1-27.
- Moran, M.S., Clarke, T.R., Inoue, Y., Vidal, A., 1994. Estimating crop water deficit using the relation between surface-air temperature and spectral vegetation index. Remote Sens. Environ. 49, 246–263.
- Mu, Q., Heinsch, F.A., Zhao, M., Running, S.W., 2007. Development of a global evapotranspiration algorithm based on MODIS and global meteorology data. Remote Sens. Environ. 111, 519–536.
- Mu, Q., Zhao, M., Running, S.W., 2011. Improvements to a MODIS global terrestrial evapotranspiration algorithm. Remote Sens. Environ. 115, 1781–1800.

### NOAA-OWP, 2016, The National Water Model.

- Oliveira, R.A., Nasi, R., Niemelainen, O., Nyholm, L., Alhonoja, K., Kaivosoja, J., Jauhiainen, L., Viljanen, N., Nezami, S., Markelin, L., Hakala, T., Honkavaara, E., 2020. Machine learning estimators for the quantity and quality of grass swards used for silage production using drone-based imaging spectrometry and photogrammetry. Remote Sens. Environ. 246, 246.
- Pastorello, G., Trotta, C., Canfora, E., Chu, H., Christianson, D., Cheah, Y.-W.,
  Poindexter, C., Chen, J., Elbashandy, A., Humphrey, M., Isaac, P., Polidori, D.,
  Reichstein, M., Ribeca, A., van Ingen, C., Vuichard, N., Zhang, L., Amiro, B.,
  Ammann, C., Arain, M.A., Ardö, J., Arkebauer, T., Arndt, S.K., Arriga, N.,
  Aubinet, M., Aurela, M., Baldocchi, D., Barr, A., Beamesderfer, E., Marchesini, L.B.,
  Bergeron, O., Beringer, J., Bernhofer, C., Berveiller, D., Billesbach, D., Black, T.A.,
  Blanken, P.D., Bohrer, G., Boike, J., Bolstad, P.V., Bonal, D., Bonnefond, J.-M.,
  Bowling, D.R., Bracho, R., Brodeur, J., Brümmer, C., Buchmann, N., Burban, B.,

Burns, S.P., Buysse, P., Cale, P., Cavagna, M., Cellier, P., Chen, S., Chini, I., Christensen, T.R., Cleverly, J., Collalti, A., Consalvo, C., Cook, B.D., Cook, D., Coursolle, C., Cremonese, E., Curtis, P.S., D'Andrea, E., da Rocha, H., Dai, X., Davis, K.J., Cinti, B.D., Grandcourt, Ad, Ligne, A.D., De Oliveira, R.C., Delpierre, N., Desai, A.R., Di Bella, C.M., Tommasi, Pd, Dolman, H., Domingo, F., Dong, G., Dore, S., Duce, P., Dufrêne, E., Dunn, A., Dušek, J., Eamus, D., Eichelmann, U., ElKhidir, H.A.M., Eugster, W., Ewenz, C.M., Ewers, B., Famulari, D., Fares, S., Feigenwinter, I., Feitz, A., Fensholt, R., Filippa, G., Fischer, M., Frank, J., Galvagno, M., Gharun, M., Gianelle, D., Gielen, B., Gioli, B., Gitelson, A., Goded, I., Goeckede, M., Goldstein, A.H., Gough, C.M., Goulden, M.L., Graf, A., Griebel, A., Gruening, C., Grünwald, T., Hammerle, A., Han, S., Han, X., Hansen, B.U., Hanson, C., Hatakka, J., He, Y., Hehn, M., Heinesch, B., Hinko-Najera, N., Hörtnagl, L., Hutley, L., Ibrom, A., Ikawa, H., Jackowicz-Korczynski, M., Janouš, D., Jans, W., Jassal, R., Jiang, S., Kato, T., Khomik, M., Klatt, J., Knohl, A., Knox, S., Kobayashi, H., Koerber, G., Kolle, O., Kosugi, Y., Kotani, A., Kowalski, A., Kruijt, B., Kurbatova, J., Kutsch, W.L., Kwon, H., Launiainen, S., Laurila, T., Law, B., Leuning, R., Li, Y., Liddell, M., Limousin, J.-M., Lion, M., Liska, A.J., Lohila, A., López-Ballesteros, A., López-Blanco, E., Loubet, B., Loustau, D., Lucas-Moffat, A., Lüers, J., Ma, S., Macfarlane, C., Magliulo, V., Maier, R., Mammarella, I., Manca, G., Marcolla, B., Margolis, H.A., Marras, S., Massman, W., Mastepanov, M., Matamala, R., Matthes, J.H., Mazzenga, F., McCaughey, H., McHugh, I., McMillan, A.M.S., Merbold, L., Meyer, W., Meyers, T., Miller, S.D., Minerbi, S., Moderow, U., Monson, R.K., Montagnani, L., Moore, C.E., Moors, E., Moreaux, V., Moureaux, C., Munger, J.W., Nakai, T., Neirynck, J., Nesic, Z., Nicolini, G., Noormets, A., Northwood, M., Nosetto, M., Nouvellon, Y., Novick, K., Oechel, W., Olesen, J.E., Ourcival, J.-M., Papuga, S.A., Parmentier, F.-J., Paul-Limoges, E., Pavelka, M., Peichl, M., Pendall, E., Phillips, R.P., Pilegaard, K., Pirk, N., Posse, G., Powell, T., Prasse, H., Prober, S.M., Rambal, S., Rannik, Ü., Raz-Yaseef, N., Rebmann, C., Reed, D., Dios, V.Rd, Restrepo-Coupe, N., Reverter, B.R., Roland, M., Sabbatini, S., Sachs, T., Saleska, S.R., Sánchez-Cañete, E.P., Sanchez-Mejia, Z.M., Schmid, H.P., Schmidt, M., Schneider, K., Schrader, F., Schroder, I., Scott, R.L., Sedlák, P., Serrano-Ortíz, P., Shao, C., Shi, P., Shironya, I., Siebicke, L., Šigut, L., Silberstein, R., Sirca, C., Spano, D., Steinbrecher, R., Stevens, R.M., Sturtevant, C., Suyker, A., Tagesson, T., Takanashi, S., Tang, Y., Tapper, N., Thom, J., Tomassucci, M., Tuovinen, J.-P., Urbanski, S., Valentini, R., van der Molen, M., van Gorsel, E., van Huissteden, K., Varlagin, A., Verfaillie, J., Vesala, T., Vincke, C., Vitale, D., Vygodskaya, N., Walker, J.P., Walter-Shea, E., Wang, H., Weber, R., Westermann, S., Wille, C., Wofsy, S., Wohlfahrt, G., Wolf, S., Woodgate, W., Li, Y., Zampedri, R., Zhang, J., Zhou, G., Zona, D., Agarwal, D., Biraud, S., Torn, M., Papale, D., 2020. The FLUXNET2015 dataset and the ONEFlux processing pipeline for eddy covariance data. In: Sci. Data, 7, p. 225.

- Pereira, L.S., Allen, R.G., Smith, M., Raes, D., 2015. Crop evapotranspiration estimation with FAO56: Past and future. Agric. Water Manag. 147, 4–20.
- Pereira, L.S., Paredes, P., Melton, F., Johnson, L., Wang, T., López-Urrea, R., Cancela, J. J., Allen, R.G., 2020. Prediction of crop coefficients from fraction of ground cover and height. Background and validation using ground and remote sensing data. Agric. Water Manag. 241, 106197.
- Prihodko, L., Goward, S.N., 1997. Estimation of air temperature from remotely sensed surface observations. Remote Sens. Environ. 60, 335–346.
- Rahman, M.S., Di, L.P., 2020. A systematic review on case studies of remote-sensing-based flood crop loss assessment. Agric. -Basel 10, 10.
- Rouse, J.W., Haas, R.H., Schell, J.A., Deering, D.W., Harlan, J.C., 1974, Monitoring the vernal advancements and retrogradation of natural vegetation. NASA/GSFC, pp. 1–137
- Senay, G., 2008. Modeling landscape evapotranspiration by integrating land surface phenology and a water balance algorithm. Algorithms 1, 1-68.

- Shroyer, J.P., Thompson, C., Brown, R., Ohlenbach, P.D., Fjell, D.L., Staggenborg, S., 1996, Kansas crop planting guide, Kansas State University, Manhattan, KS.
- Su, B., 1988. The surface energy balance system (SEBS) for estimation of turbulent heat fluxes. Hydrol. Earth Syst. Sci. 6.
- Sun, H., 2015. Two-stage trapezoid: a new interpretation of the land surface temperature and fractional vegetation coverage space. IEEE J. Sel. Top. Appl. Earth Obs. Remote Sens. 9
- Sun, J., Lai, Z.L., Di, L.P., Sun, Z.H., Tao, J.B., Shen, Y.L., 2020a. Multilevel deep learning network for county-level corn yield estimation in the US corn belt. Ieee J. Sel. Top. Appl. Earth Obs. Remote Sens. 13, 5048–5060.
- Sun, Z.H., Di, L.P., Fang, H., Burgess, A., 2020b. Deep learning classification for crop types in North Dakota. Ieee J. Sel. Top. Appl. Earth Obs. Remote Sens. 13, 2200–2213
- Tang, R., Li, Z., 2017. An end-member-based two-source approach for estimating land surface evapotranspiration from remote sensing data. IEEE Trans. Geosci. Remote Sens. 55. 5818–5832.

#### USGS, 2010. Evapotranspiration and the Water Cycle.

- Virnodkar, S.S., Pachghare, V.K., Patil, V.C., Jha, S.K., 2020. Remote sensing and machine learning for crop water stress determination in various crops: a critical review. Precis. Agric. 21, 1121–1155.
- Wang, K., Dickinson, R., 2012. A review of global terrestrial evapotranspiration: observation, modeling, climatology, and climate variability. Rev. Geophys. 50, RG2005.
- Wardlow, B.D., Egbert, S.L., Kastens, J.H., 2007. Analysis of time-series MODIS 250 m vegetation index data for crop classification in the US Central Great Plains. Remote Sens. Environ. 108, 290–310.
- Wilson, K., Goldstein, A., Falge, E., Aubinet, M., Baldocchi, D., Berbigier, P., Bernhofer, C., Ceulemans, R., Dolman, H., Field, C., Grelle, A., Ibrom, A., Law, B.E., Kowalski, A., Meyers, T., Moncrieff, J., Monson, R., Oechel, W., Tenhunen, J., Valentini, R., Verma, S., 2002. Energy balance closure at FLUXNET sites. Agric. For. Meteorol. 113. 223–243.
- Xia, Y., Hobbins, M., Mu, Q., Ek, M., 2015. Evaluation of NLDAS-2 evapotranspiration against tower flux site observations. Hydrol. Process. 29, 29–1771.
- Xia, Y., Mitchell, K., Ek, M., Sheffield, J., Cosgrove, B., Wood, E., Luo, L., Alonge, C., Wei, H., Meng, J., Livneh, B., Lettenmaier, D., Koren, V., Duan, Q., Mo, K., Fan, Y., Mocko, D., 2012. Continental-scale water and energy flux analysis and validation for the North American Land Data Assimilation System project phase 2 (NLDAS-2): 1. Intercomparison and application of model products. J. Geophys. Res.: Atmos. 117, 117-n/a.
- Xu, J.F., Zhu, Y., Zhong, R.H., Lin, Z.X., Xu, J.L., Jiang, H., Huang, J.F., Li, H.F., Lin, T., 2020. DeepCropMapping: a multi-temporal deep learning approach with improved spatial generalizability for dynamic corn and soybean mapping. Remote Sens. Environ. 247.
- Xue, J., Bali, K., Light, S., Hessels, T., Kisekka, I., 2020. Evaluation of remote sensing-based evapotranspiration models against surface renewal in almonds, tomatoes and maize. Agric. Water Manag. 238, 106228.
- Yang, Y., Chen, S., Zhang, R., Tian, J., Li, L., 2015. An enhanced two-source evapotranspiration model for land (ETEML): algorithm and evaluation. Remote Sens. Environ. 168, 54–65.
- Yu, B., Shang, S., Zhu, W., Gentine, P., Yu, C., 2019. Mapping daily evapotranspiration over a large irrigation district from MODIS data using a novel hybrid dual-source coupling model. Agric. For. Meteorol. 276–277, 107612.
- Zhang, C., Di, L., Lin, L., Guo, L., 2019. Machine-learned prediction of annual crop planting in the U.S. corn belt based on historical crop planting maps. Comput. Electron. Agric. 166, 104989.